Chapter 5

Mechanisms controlling interfacial $Ce_{0.9}Gd_{0.1}O_{2-y}$ nanostructures growth: *experimental approach*

The ability to finely tune interfacial nanoislands' shape through the accurate control of growth conditions together with the use of ultradiluted metal-organic solutions turns $Ce_{0.9}Gd_{0.1}O_{2-y}/LaAlO_3$ (CGO/LAO) into a very singular and appealing system. Such control of CGO nanostructures formation results into well-localized nanodots and highly elongated orthogonal nanowires, just by leaving the system evolve to its configuration of lower energy. So, CGO/LAO arises as an excellent candidate to investigate self-assembling and self-organized processes in chemical solution derived nanostructured templates. These bottom-up methodologies have already been intensively investigated as efficient nanostructuring routes in semiconductors [12, 13] and metals [46, 72, 73], though they are just spreading to other emergent fields such as oxide nanotechnology. On the other hand, the deposition of chemical solutions to generate interfacial nanoislands also constitutes an innovative challenge, since till the moment vacuum related techniques were nearly exclusively used. Moreover, knowledge of the mechanisms driving the island to adopt a square or rectangular shape might as well provide us with a very general and useful tool to tune the lateral aspect ratio of interfacial nanoislands.

In addition to the interest in CGO/LAO as a model oxide system to study kinetic and equilibrium mechanisms in interfacial oxide nanostructures, CGO itself is a key material of high intrinsic interest in many areas such as catalysis, ionic conductivity, optical and dielectric properties, buffer layer for oxide thin films and nanostructured template for manipulation of vortex properties in superconductor materials, etc. [76, 224, 241-243]. Hence, it appears as highly demanding, scientifically and technologically, to study in detail the mechanisms generating nanostructured networks of CGO.

In this chapter, we search for an experimental answer to most of the questions aroused after the singular behaviour observed in interfacial CGO-nanostructures under different growth

conditions (section 4.3). A detailed study of these templates, CGO/LAO, is presented in order to resolve the structural characteristics that lead to the growth of islands with isomorphic or elongated in-plane shape. Their contrasted evolution paths, characterized by stable nanodots or by the continuous coalescence of wires respectively, are also extensively investigated. Whereas in the present chapter description of CGO nanostructures is based on experimental research, next chapter 6 will complete these results through thermodynamic analyses based on the energies involved in the system.

5.1 Morphology and crystallographic orientation of CGO nanoislands

As described beforehand, at first glance, one of the most outstanding features of fluorite CGO nanoislands grown on perovskite LAO single-crystals is their differences in morphology according to their particular growth conditions. At elevated temperatures, isomorphic nanoislands characterize templates annealed in high oxidizing atmosphere; whereas the use of a reducing atmosphere enhances the formation of highly elongated nanostructures (nanowires). Two typical examples are displayed in Fig. 5-1. Both templates were prepared from 0.008 M metal-organic solution and processed at 1000°C for 15 minutes; one in O_2 (Fig. 5-1a) and the other in Ar-5%H_2 (Fig. 5-1b). Thus, dots and wires are the resulting interfacial nanostructures, respectively. So, we must investigate what makes some islands elongate whereas others remain with isomorphic shape.

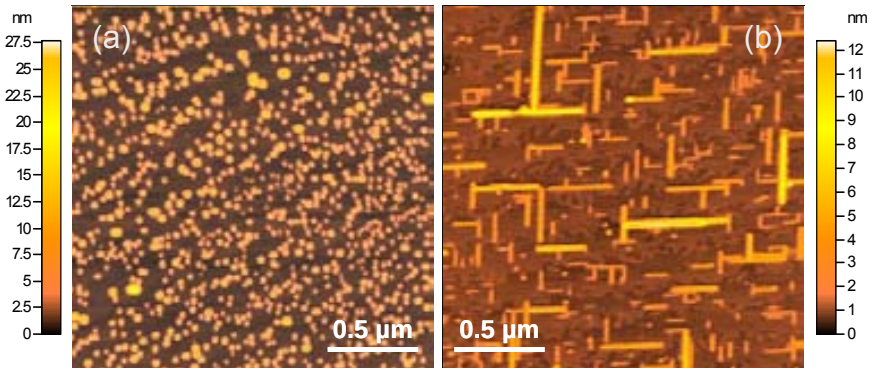

Fig. 5-1: Isomorphic CGO nanodots (a) and elongated CGO nanowires (b). AFM topographic images correspond to two CGO/LAO templates processed at 1000°C for 15 min in O_2 (a) and Ar-5%H_2 (b). Metal-organic 0.008M precursor solutions were used.

A structural analysis points out that the contrast between these two kinds of nanostructures is essentially due to their particular crystallographic orientation, which results to be one of the main sources of the distinct shapes and evolution paths followed by the islands. In next paragraphs, this structural characterization based on XRD, TEM, HRTEM and RHEED is presented. Synchrotron X-ray diffraction experiments are planned to analyze the anisotropic strain distribution of the different type of nanostructures obtained.

5.1.1 Isomorphic CGO nanostructures

At 1 bar of pure oxygen pressure, CGO-nanostructures grow epitaxially on LAO substrates with the expected orientation (001)CGO||(001)LAO. These results are shown in (111)-CGO pole figure displayed in Fig. 5-2a, where there appear four peaks at χ~54° corresponding to the angle between (111) and (100)-planes. CGO-(111) peaks are localized at ϕ values separated 90° as corresponds to the fluorite structure though rotated 45° in respect to (111)-LAO peaks (Fig. 5-2b), indicative that fluorite CGO structure grows rotated 45° about [001]-LAO axis, i.e. CGO[110]||LAO[100].

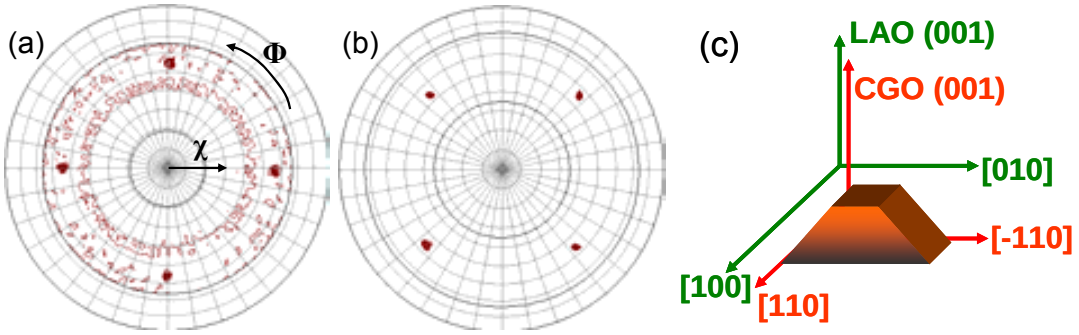

Fig. 5-2: XRD[2] analysis of interfacial CGO nanodots on LAO substrates grown in high oxidizing atmosphere at 1000°C revealing a (001)CGO[110]||(001)LAO[100] epitaxial orientation: (111)-CGO (a) and (111)-LAO (b) pole figures. A schema of this orientation is shown in (c).

As observed in AFM image in Fig. 5-1a and in many examples in section 4.3, nearly all CGO nanoislands processed in O_2 are isomorphic in in-plane shape. So, we have proved that CGO isomorphic nanodots are (001)-oriented. Such results have been confirmed in a large number of CGO/LAO templates processed in oxidizing atmosphere. A schematic representation of this configuration for a (001)CGO dot on LAO substrate is depicted in Fig. 5-2c.

Accordingly to lattice site model [193], (001)CGO[110]||(001)LAO[100] is the lowest lattice mismatch configuration, ε~-1%. A well-matching of oxygen sublattices is appreciated in the solid spheres model displayed in Fig. 5-3a. However, in the corresponding planar-view (Fig. 5-3b) it is observed that oxygen vacancies must be created at the interface because there is not enough room to fit all oxygen of both crystallographic structures. They should be separated 1.35 Å, but oxygen ionic radius is already 1.4 Å [244]. In both pictures, just simple fluorite CeO_2 structure free of Gd has been considered and, thus, oxygen vacancies resulting from Gd^{3+} doping are not drawn. Therefore, in the heteroepitaxial growth of dissimilar oxide structures (i.e. fluorite/perovskite) the misfit between cations must be investigated instead of the misfit between oxygen sublattices as it is typical assumed in oxides [192]. This fact has recently been pointed out by Garcia-Barriocanal *et al.* [159]. They signalled the formation of oxygen vacancies at the interface of highly dissimilar structures like perovskite and fluorite as the

mechanism yielding to colossal values of ionic conductivity at interface of epitaxial ZrO_2:Y_2O_3/$SrTiO_3$ heterostructures.

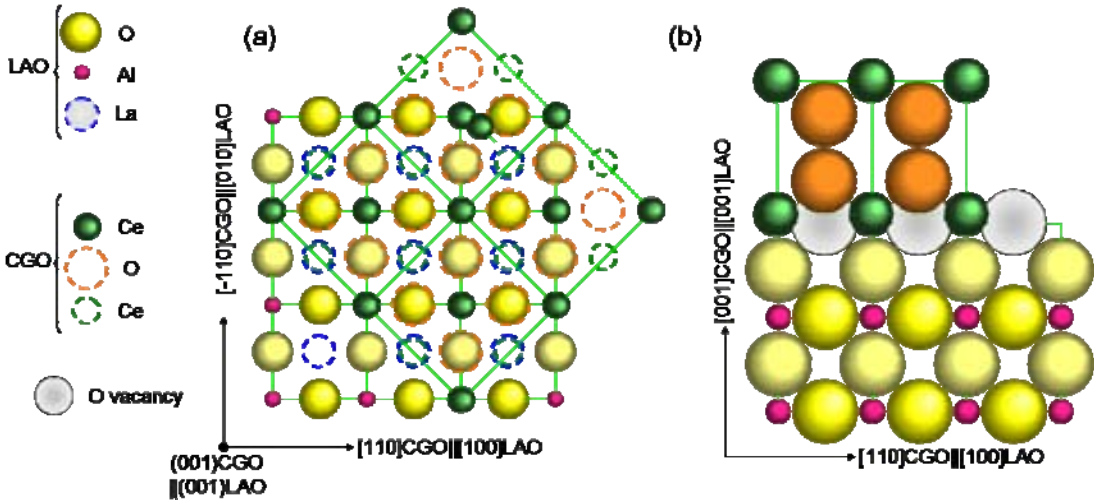

Fig. 5-3: Solid spheres model showing the configuration (001)CGO[110]||(001)LAO[100]. Planar-view (a) proves the compatibility between fluorite-CGO (rotated) and perovskite-LAO; the colourful spheres correspond to atoms located at the interface, whereas atoms belonging to upper or lower positions are represented as dashed circles. Side view (b) where just planes (100)-LAO and (110)-CGO are represented. An overlap of oxygen atoms at the interface is observed, indicating that oxygen vacancies must be created (grey spheres). The ionic radius of spheres in the planar-view is reduced up to 60% for a better visualization. Gd atoms and oxygen vacancies resulting from this doping are not drawn.

Fig. 5-4 displays a typical TEM cross-section image of a nanodot (001)CGO[110]||(001)LAO[100] viewed along <100>LAO zone axis, where it is observed that CGO/LAO interface is sharp and well-defined, without intermediate layers. This specific nanodot is about 8.5 nm wide and 4.2 nm high. This size is smaller than those typically determined by AFM, where convolution effects of the tip are present.

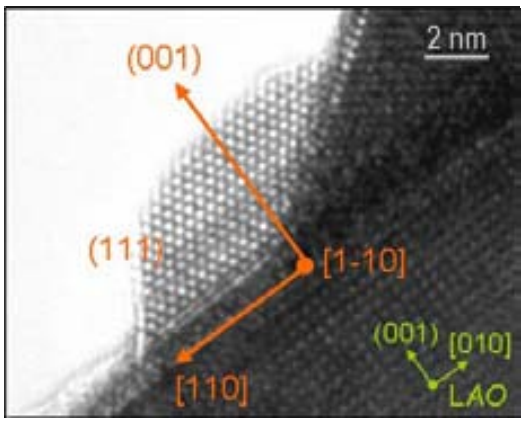

Fig. 5-4: TEM cross-section image corroborating (001)CGO[110]||(001)LAO[100] orientation of a CGO-nanodot processed in oxidizing atmosphere at 1000°C, viewed along <100> LAO zone axis. Lateral (111) facets and truncated shape is observed.

Information about the degree of relaxation of islands is typically obtained comparing the mean separation between dislocations observed in TEM images with the theoretical value

required to achieve full relaxation of the system. The separation between misfit dislocations in a fully relaxed bulk system is computed as [245, 246]

$$S = \frac{|\vec{b}|}{\varepsilon} \qquad \textbf{Eq. 5-1}$$

where |**b**| is the modulus of Burgers vector and ε the lattice mismatch. In the present case, |**b**|=½<110> leads to S~36 nm. This value indicates that the mean separation between dislocations in a fully relaxed island should be larger than the size of nanodots themselves and, thus, there is no point in investigating the degree of relaxation of these nanodots. Since the mismatch for (001)CGO[110]||(001)LAO[100] is small, the strain energy of this system is also expected to be small.

For (001)CGO dots, both in-plane growing directions, i.e. [110]CGO||[100]LAO and [-110]CGO||[010]LAO, are equivalent from a misfit point of view. Therefore, in-plane elongation does not seem to result in any benefit for (001)-dots from elastic relaxation perspective. So, (001)-dots' growth takes place in a cubic anisotropic media or, more simply, it can be considered that nanodots are biaxial isotropic stressed.

Lateral facets of (001)-nanodots are identified as (111) planes, inclined (54±2)^{o} with respect to the substrate (Fig. 5-4). So, (001)-dots are faceted pyramids with a square base, instead of being round-shaped as previously derived from AFM images. This morphology can clearly be appreciated in TEM planar-view displayed in Fig. 5-5a. In these views, most artefacts typically observed in AFM topographic images, especially due to tip's convolution, are eliminated. A square-based nanodot is observed at the centre of the image; microdiffraction analysis of this high resolution TEM (Fig. 5-5b) proved that it effectively corresponds to a (001)-oriented CGO dot.

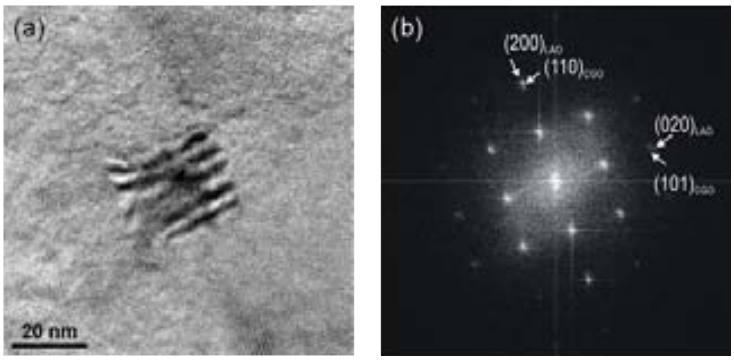

Fig. 5-5: TEM planar-view image where the isomorphic square base of a (001)CGO nanodot is clearly appreciated (a); microdiffraction analysis proving the epitaxial relation (001)CGO[110]||(001)LAO[100] of this dot (b).

Molecular mechanics calculations of surface energies for different facets of CeO_2 yielded to the following surface energy correlation after relaxation of atomic positions [247, 248]

$$\{111\} < \{110\} < \{211\} < \{100\} < \{210\} < \{310\}$$ **Relation 5-1**

{111} surface is the one with lowest energy and the most stable, because its surface atoms have the lowest coordination deficiency and it is also the most compact. Consequently, by choosing {111} planes as lateral facets, (001)CGO islands are minimizing their surface energy. So, in-plane isomorphic shape can be expected for (001)-dots from a surface energy point of view, since all lateral facets are equivalent and, hence, there is no instigator promoting island elongation to achieve a lower energy configuration.

No triangular cross-section is observed among all (001)-dots examined by TEM. Instead, they are ended in flat (001)-CGO planes, indicating a pyramidal truncated shape for (001)CGO nanodots (i.e. Fig. 5-4). Fig. 5-6 shows the dependence of dots' height with half of its lateral size, h(a/2); data is obtained from TEM cross-section images like the one displayed in Fig. 5-4. Experimental values (blue round symbols) are compared with the height that would have dots of the same lateral size but with triangular cross-section instead of being truncated; in this case, the height is trigonometrically calculated knowing that lateral facets are bevelled 54°. Both lines cross at very small sizes (a/2<0.5 nm), suggesting that (001)-dots are truncated since very initial stages of growth, perhaps since nucleation. This may explain why any pointed (001)-dot is observed in TEM cross-section images.

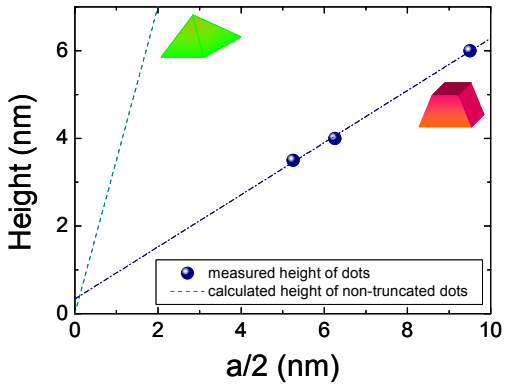

Fig. 5-6: Height of (001)CGO dots as function of half of its lateral size, h(a/2) (●); data is obtained from TEM cross-section images. Dashed line (--) indicates the calculated height of a non-truncated dot with same lateral size. Cross-over between both curves occurs for island's sizes a/2<0.5 nm.

From polar solid principles, a crystal surface plane can only exist if there is a zero electrical dipole component normal to the surface [248-250]. Therefore, a {100}-CGO surface would not be possible because a net dipole perpendicular to it remains after a mere geometric cleaving of crystal lattice. However, it has been pointed out that if 50% of oxygens from the outer layer are removed in order to suppress charge excess, the zero dipole energetic requirement is achieved and {100}-$Ce_{1-x}Gd_xO_{2-y}$ surface becomes physically stable [248]. Thus, (001)-CGO is a stable surface.

Summarizing, (001)CGO nanodots can be described at first approximation as square-based pyramids with (111) lateral facets and flat-ended in (001) planes, which grow biaxial isotropic strained according to the epitaxial relation (001)CGO[110]||(001)LAO[100]. Once crystallographic orientation, facets and lattice mismatch of oxygen-processed nanodots is determined, a theoretical study can be carried out to investigate the equilibrium shape of these nanoislands. Consequently, a thermodynamic analysis mainly based on surface and elastic relaxation energies will be presented in next chapter 6.

5.1.2 Elongated CGO nanowires

Let's focus now on CGO/LAO templates just bearing strong interfacial anisotropic nanoislands (long axis *b* > short axis *a*), which are those processed in reducing atmosphere (Fig. 5-1b). In the corresponding (111)-CGO pole figure shown in Fig. 5-7a, four peaks are observed at $\chi \sim 35^{o}$ and oriented at ϕ values separated by 90^{o}. The position χ of these peaks indicates that elongated nanostructures, i.e. *nanowires*, are unexpectedly oriented (011)CGO||(001)LAO. This particular crystallographic orientation was already observed in ~79% of the volume of CGO/LAO thin films prepared from CSD and processed in reducing atmosphere (see section 4.3.3).

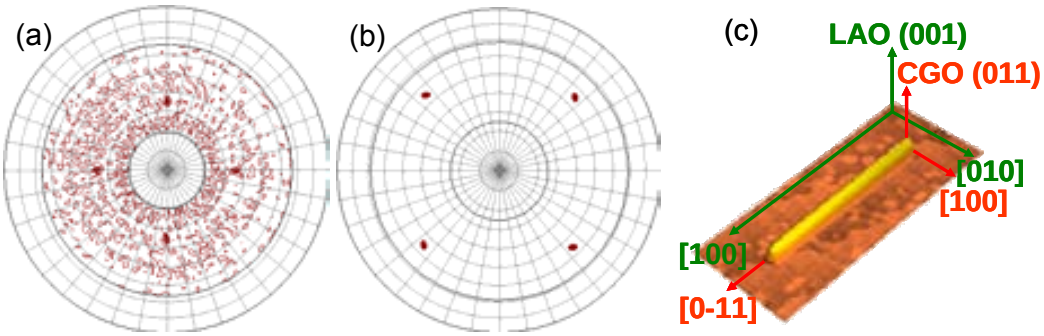

Fig. 5-7: XRD[2] analysis of interfacial CGO nanowires on LAO substrates grown in reducing atmosphere at 1000°C, i.e. Ar-5%H_2: (111)-CGO (a) and (111)-LAO pole figure (b) evidences (011)CGO[0-11]||(001)LAO[100] orientation of wires. A schematic representation (c) of this orientation for a single wire is also shown, in agreement with TEM analysis presented in Fig. 5-9.

Directions orthogonal to [011] are [100] and [0-11]. Therefore, this epitaxial relation implies two distinct in-plane growth directions, CGO[100]||LAO[100] and [0-11]CGO||[010]LAO, as determined in agreement with (111)-LAO pole figure displayed in Fig. 5-7b. The two-fold multiplicity of the reflection (111) for that particular (011)-CGO crystallographic orientation would result in just two peaks in pole figure spectra. The apparition of four peaks (Fig. 5-7a) is consequence of the existence of two in-plane degenerate orientations for wires' growth, i.e. (011)CGO[0-11]||(001)LAO[010] and (011)CGO[0-11]||(001)LAO[100].

That explains why two equivalent families of nanowires orthogonally in-plane oriented are observed.

In collaboration with IFW-Dresden, RHEED analysis of CGO nanowires grown on LAO single-crystals substrates were carried out. Two different orientations of the electron beam with respect to the substrate were investigated, <100> and <110>. In both cases, the diffraction pattern was compared to that of a bare substrate in order to identify the contribution of CGO nanoislands. The experimental diffraction patterns corresponding to the two electron beam orientations are displayed in Fig. 5-8a and b. Both of them are spotty patterns as it is expected for surfaces with 3D islands. A full indexation of the diffraction pattern is achieved when considering the epitaxial relationship (011)CGO[0-11]||(001)LAO[010] as well as (001)CGO[110]|| (001)LAO[100]. Whereas the former is required for the full indexation of patterns corresponding to templates with nanowires, the latter is indistinguishable from a bare LAO substrate. This matching is observed in Fig. 5-8c and d, where experimental and simulated patterns are simultaneously displayed including both simulated orientations for CGO and LAO. Instead, Fig. 5-8e and f just displays simulated patterns to avoid confusion. Therefore, RHEED measurements confirm that patterns corresponding to wire-nanostructured templates are characteristic of (011)-CGO crystallographic orientation.

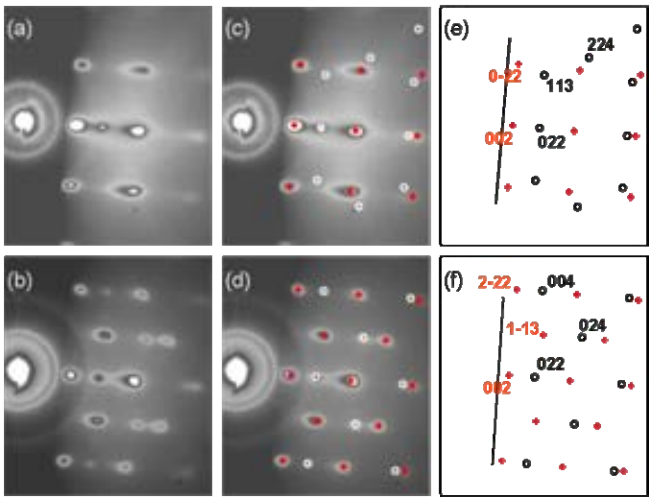

Fig. 5-8: RHEED diffraction patterns of CGO nanoislands grown on LAO substrate: Experimental pattern with the electron beam directed along <100> (a) and <110> (b). Indexed (c and d) and simulated (e and f) patterns corresponding to CGO (dot symbols) following the orientation (011)CGO[0-11]||(001)LAO[100], and LAO together with (001)CGO[110]||(001)LAO[100] dots (red cross symbols).

Fig. 5-9 shows a TEM cross-section image of a CGO/LAO template grown in reducing atmosphere at 1000^{o}C where two (011)CGO nanowires are viewed along <100>LAO substrate zone axis. One nanowire is cut along its long axis and the other orthogonally to it. From this image, it is revealed that elongation takes place along CGO[0-11]||LAO[010] direction, whereas nanowire's short axis is aligned with CGO[100]||LAO[100]. A schematic representation of this

configuration is drawn in Fig. 5-7c. In addition, HRTEM analysis resolves that long lateral facets of nanowires correspond to (111) planes, while short axes are limited by (100) planes, bevelled 35º and 45º to the substrate, respectively. Taking into account the surface energies of CeO_2 exposed in Relation 5-1, nanowires elongate maximizing the side of lower surface energy; that is, (111) facets. So, in contrast to (001)-dots, (011)-nanowires exhibit lateral facets of different surface energy, which already suggests one possible reason for islands' elongation, i.e. minimization of surface energy.

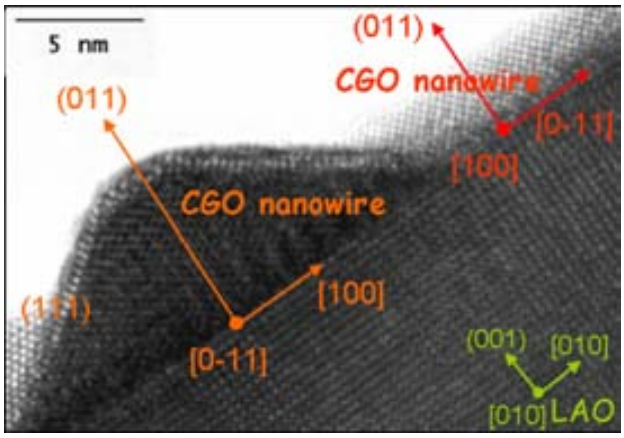

Fig. 5-9: TEM cross-section image of two (011)CGO nanowires cut along (right side) and perpendicular (left side) to their long axis viewed along <100> LAO zone axis.

Lattice mismatch computed through the coincidence of cation sublattices along [0-11]CGO||[010]LAO yields to ε~-1%. Mismatch in this direction is the same exhibited by (001)-nanodots (section 5.1.1). In the present case, mean separation between dislocations could neither be experimentally determined due to the difficulty to obtain a cross-section TEM image of the whole length of a nanowire (typically, >80 nm).

For the epitaxial growth along [100]CGO||[100]LAO, the mismatch crystalline axis determined from the comparison of lattice parameters would be ε~-30%. No physical meaning can be attributed to this misfit, since no coherent growth would be possible under such strain in the framework of low misfit epitxay (LME). Instead of matching the same planes or lattice constants (LME), domain matching epitxay (DME) model proposes the accommodation of misfit by matching of integral multiples of lattice planes and the existence of one dislocation corresponding to each domain [194]. Accordingly, DME states that epitaxial growth is possible for any misfit. For example, the growth of TiN on (100)-Si was demonstrated by DME alternating 3/4 and 4/5 domains, despite the existence of a misfit of 22% for the cube-on-cube growth. In the case that the matching of integral multiples is not perfect, DME leaves a residual misfit computed as

$$\varepsilon_r = \left(\frac{m\, d_F}{n\, d_S} - 1 \right) \qquad \textbf{Eq. 5-2}$$

where d_F and d_S are the distances between matching planes of the deposited material and the substrate, respectively, and m and n are the integers describing the domain matching relation. For the case of [100]CGO||[100]LAO, there exists a good 2/3 matching relation, i.e. 2 fluorite cells fit pretty well 3 perovskite cells, as is illustrated in Fig. 5-10 through a model of solid spheres. Accordingly, DME proposes a 2/3 domain structure with the formation of a dislocation in each domain and the existence of a residual misfit $\varepsilon_r \sim +5\%$ (determined from Eq. 5-2 considering n=2 and m=3).

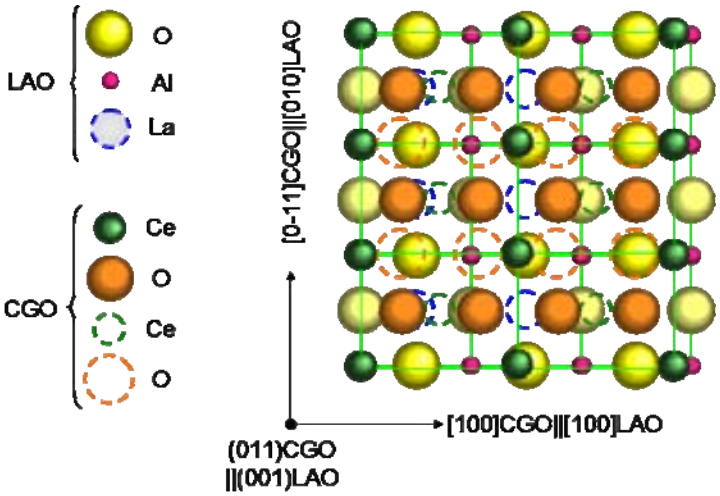

Fig. 5-10: Solid spheres model showing a planar-view of the compatibility of the growth of (011)CGO[0-11]||(001)LAO[010]. Pretty good matching is achieved along CGO[0-11]||LAO[010], whereas a 2/3 domain matching relation applies along CGO[100]||LAO[100]. Colourful spheres correspond to the atoms localized at the interface, whereas the circles indicate atoms localized below or above it. For a better visualization, spheres' radius is reduced up to 60% of the corresponding ionic radius.

Corroboration of the suitability of DME model to describe the epitaxial growth of (011)CGO wires along [100]CGO||[100]LAO (i.e., their short axis) can be obtained from analyses of TEM cross-section images based on Burgers circuits, like the ones exhibited in Fig. 5-11. A Burgers vector **b** is a crystal vector which quantifies the difference between the distorted lattice around a dislocation and the perfect lattice [251]. A Burgers circuit is built-up by tracing a close loop around the end of a dislocation plane. Due to the distortion, the number of lattice vectors travelled in one side of the interface differs from the other one; the vector difference (i.e., closure failure when same number of lattice vectors is travelled along both sides) corresponds to the Burgers vector. Two Burgers circuits have been drawn around the (011)CGO[100]||(001)LAO[100] interface displayed in Fig. 5-11. Burgers vectors **b**=a<100> are required to close them. Particularly, in green Burgers circuit it is found that 2 CGO unit-cells fit 3 LAO unit-cells, satisfying the proposed 2/3 domain matching relation. Red circuit

shows that 4 fluorite unit-cells match 6 perovskite unit-cells; so, the same 2/3 relation is fulfilled. Application of DME model would also imply the formation of a dislocation every domain. Dislocations are difficult to see in Fig. 5-11; however, advanced analyses can help to easily observe them.

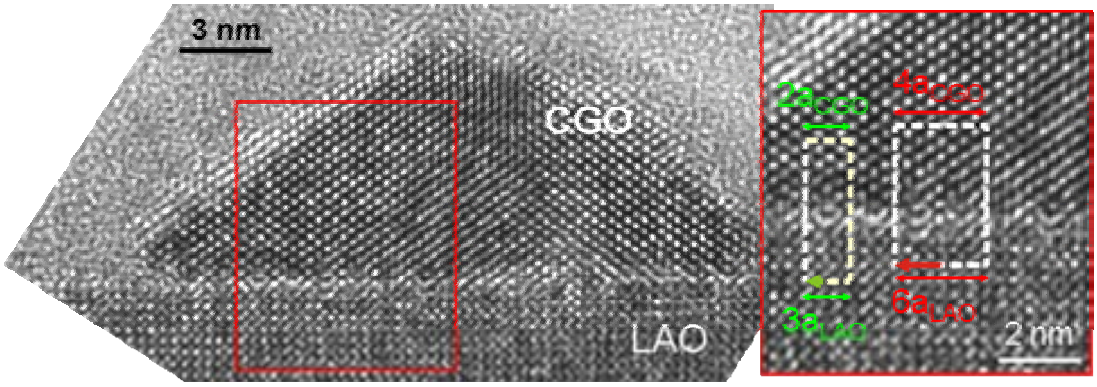

Fig. 5-11: High resolution TEM cross-section image of a (011)CGO nanowire cut along its short axis, viewed along <010>LAO zone axis. Burgers circuits around the interface (inset on the right) confirm a 2/3 domain matching relation between the fluorite CGO and perovskite LAO along [100]CGO||[100]LAO.

Better visualization of interface in Fig. 5-11 can be achieved performing an inverse-FFT (IFFT), as it is shown in Fig. 5-12. This image is obtained with the (200) spots of CGO and (100) spots of LAO of FFT of image in Fig. 5-11. As a result of this choice, every two observed planes of CGO in the IFFT image constituted one unit-cell of the fluorite, whereas for the case of the substrate the separation between planes already corresponds to a LAO unit-cell. Any other plane outside of the island and the substrate is an artefact. A domain matching 2/3 is clearly observed in most of the interface (domains indicated by orange arrows); in fact, just few exceptions are observed (signalled with green arrows). In each domain, there is one extra plane (dislocation) as predicted by DME; two of them are indicated with ⊥ in Fig. 5-12. So, domain matching epitaxy model arises as a more appropriate tool to describe this particular interface, (011)CGO[100]||(001)LAO[100], than conventional misfit theory. Accordingly, strain misfit along this in-plane growing direction might probably be $\varepsilon \sim 5\%$, as determined from Eq. 5-2. In some specific points, where the number of dislocations is higher than predicted by DME a higher level of relaxation could be achieved. However, IFFT image in Fig. 5-12 shows that in eighteen 2/3 matching domains there are just two exceptions (green arrows). DME also proposes that by variations of the domain size (i.e. modification of integral multiples of lattice parameter) it is possible to accommodate any additional misfit; however, it does not seem to exactly apply to present interface since the observed modifications of domain size are not periodic.

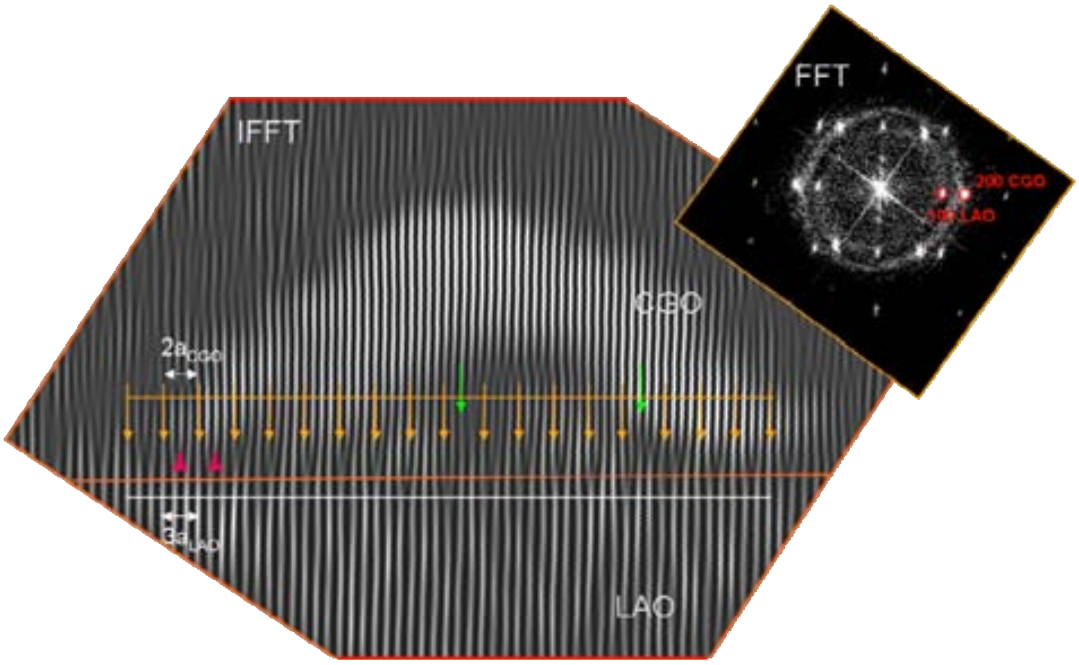

Fig. 5-12: Inverse-FFT (IFFT) image generated with the (200) spots of FFT of CGO and (100) ones of LAO of the TEM image displayed in Fig. 5-11. A domain matching relation 2/3 is indicated by orange arrows; in each domain there is a dislocation (two of them are indicated with ⊥). The only two exceptions to this pattern observed in this interface are pointed by green arrows.

Theoretical computations based on first principles are required to exactly know where and how the atoms of both structures are localized in this complex interface CGO[100]||LAO[100]. We can suggest a possible picture, like the one sketched in Fig. 5-13. Every two CGO fluorite cells a row of Ce cations should disappear at the interface to fit the LAO perovskite substrate, i.e. a dislocation would be created and the domain matching proposed by DME would be satisfied. Moreover, as it was pointed out for the epitaxial growth

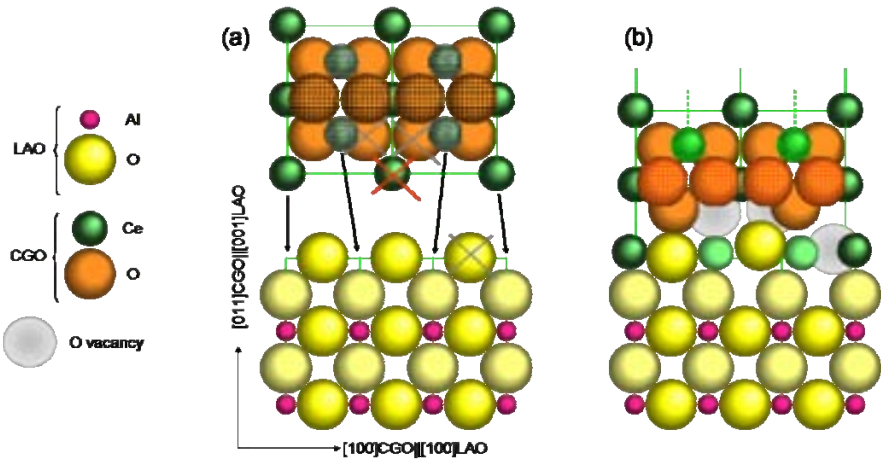

Fig. 5-13: Rough draft based on solid spheres model of a suggested reconstruction of interface CGO[100]||LAO[100]: sketch of fluorite and perovskite structures separately (a) and example of a possible resolution of the interface (b). A 2/3 domain epitaxy applies, with the formation of a dislocation in each domain (centre of the drawing) and creation of oxygen vacancies. To achieve this configuration atoms crossed in picture (a) have been removed in (b). Gridded-atoms indicate those which do not belong to the plane drawn.

along CGO[110]||LAO[100], high concentration of oxygen vacancies should be present at the interface since there is not enough space for all the oxygens. It must be noticed then that oxygen vacancies at the interface are a fact independently of the particular reconstruction of the interface, due to the dissimilarity between fluorite and perovskite structures.

Further information about this interface can be obtained from Moiré's fringes observed in TEM planar-views. Moiré fringes are an interference pattern created, for example, when two grids overlap at an angle or they have slightly different mesh sizes [252]. Fig. 5-14 shows two orthogonal (011)-nanowires where Moiré's fringes are clearly appreciated along nanowires' main axis (Fig. 5-14a), particularly after IFFT (Fig. 5-14b). Results indicate that lattice parameter of CGO along nanowires' long axis coincides with that of LAO and no Moiré pattern arise corresponding to these families of planes. Such coherent growth is in agreement with small lattice mismatch along this direction CGO[0-11]||LAO[010], i.e. ε~-1%. The apparition of fringes along wires' long axes indicates a high degree of relaxation of CGO lattice cell on LAO along CGO[100]||LAO[100], and in any case the 30% misfit strain as would be derived from LME. A mean separation between fringes d_M ~1.27-1.33 nm is measured. The spacing *d* between Moiré fringes corresponding to the overlap of two families of planes with lattice spacings d_1 and d_2, respectively, can be calculated through the equation

$$d = \frac{d_1 d_2}{|d_1 - d_2|} \qquad \textbf{Eq. 5-3}$$

Thus, a_{CGO}=5.41 Å and a_{LAO}=3.79 Å leads to a calculated mean separation *d*=1.27 nm, confirming the high degree of relaxation of CGO along nanowires' short axis. Therefore, domain matching epitaxy model seems to apply finely to the whole nanowires' length and it is not restricted to a particular cross-section image. Moiré fringes have also been observed along elongated GaAs nanocrystals on (100)Si as consequence of semi-coherent growth [64].

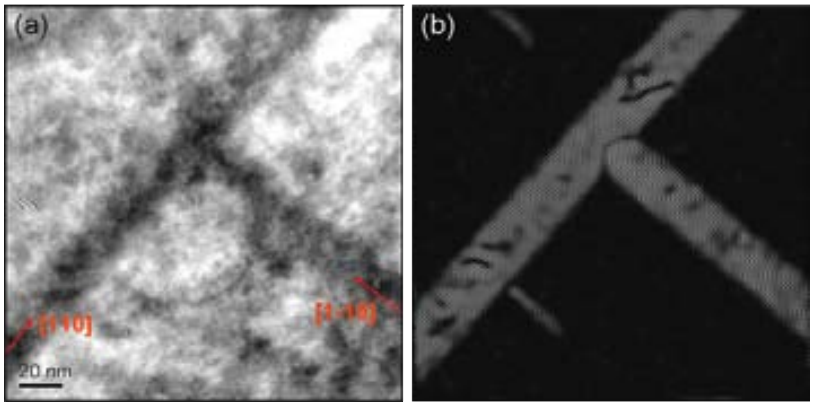

Fig. 5-14: TEM planar-view image of two orthogonal (011)-nanowires. Moiré's fringes along nanowires' main axis are clearly visible (a), and particularly in IFFT image generated using both (110) spots of corresponding FFT.

Hence, (011)-nanowires are biaxial anisotropic stressed: misfit strain is larger along their short axis than along their long axis. Therefore, elongation in the direction chosen by wires might minimize the strain energy of the system. This in-plane strain anisotropy is another important difference with respect (001)-dots, which on the contrary are submitted to the same very low lattice mismatch in both in-plane growing directions.

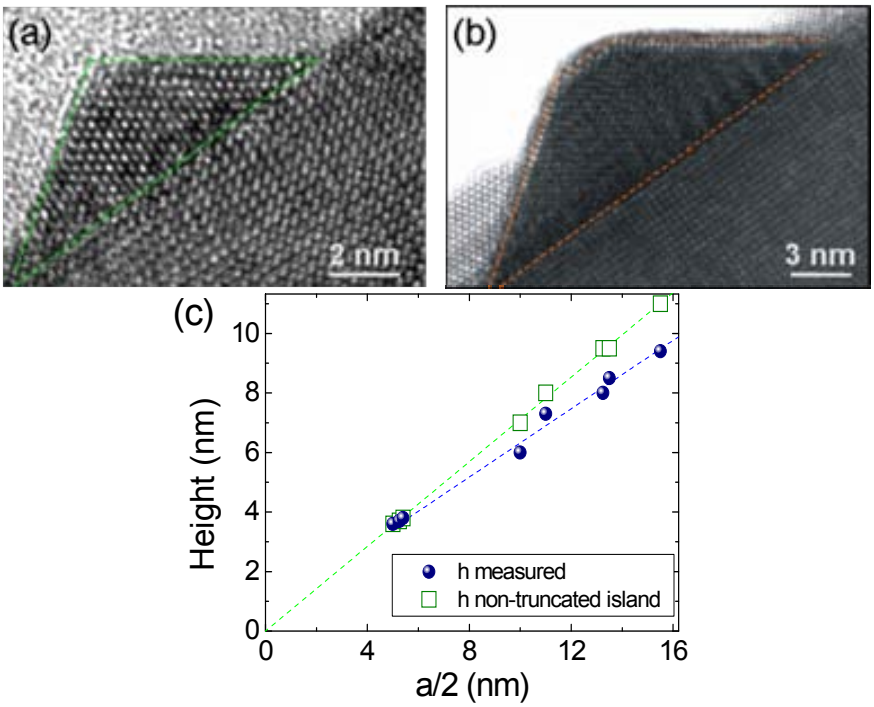

Fig. 5-15: Nanowire's vertical shape transition: from triangular cross-section (a) to truncated (b) nanowires; TEM cross-section images are viewed along <100>LAO zone axis. Plot of wires' height as function of half of their width, h(a/2) (c); close symbols (●) correspond to experimental data and open ones (□) to trigonometrically calculated heights of non-truncated islands. At low sizes (i.e. a/2<8 nm), both data coincides.

In general, it is observed that small nanowires exhibit a triangular cross-section; i.e. lateral facets sharply meet at island's top. In contrast, for large nanowires, the (011) surface develops at island's top after truncation of (111) facets. Truncation of elongated-pyramids has also been reported for the microfaceting of CeO_2 thin films grown on sapphire by sputtering after annealing [195]. This different termination of (011)CGO wires depending on their size is appreciated in high resolution TEM cross-sections images displayed in Fig. 5-15, where both shapes are exemplified in figures (a) and (b), respectively. From TEM cross-section images of distinct wires, the relation between wires' height and its width is determined. Fig. 5-15c displays the plot height *vs.* half of wires' short axis width, h(a/2). Close symbols correspond to measured sizes, whereas the open ones indicate the height of a wire with same short axis but point ended (determined through trigonometric relations). For small heights and sizes, the slope of that plot ~0.71 coincides with the expected for pyramidal islands $tg(35^o)=0.70$; i.e. open and close symbols match. However, for a/2>8 nm (which corresponds to h~5 nm) wires' height

starts to grow slower and deviates from this relation, indicating the moment when the wires become truncated. As a result, a general relation between island's height and width is extracted; evidencing a link between these two island dimensions. Specifically, wires's width grows faster than its height, behaviour which is stressed after truncation. The transition from sharp to flat island crests is sometimes associated with the introduction of misfit dislocations at the interface, initiating plastic strain relaxation and slowing down vertical growth [38]. However, in the present case, the same stage of strain described along [100]CGO||[100]LAO is observed for both configurations.

A TEM planar-view of a CGO/LAO template processed 10 min in Ar-H_2 at 1000^{o}C is displayed in Fig. 5-16. Without AFM's tip convolution effects, nanowires' short axis size *a* can be much accurately determined. In general, its short axis is much thinner than that observed in AFM images. It is because this artefact exaggeratedly masks objects with dimensions close to tip's radius size, which explains why no significant differences are observed in long axes lengths. As consequence, nanowires actually have even larger in-plane aspect ratios (long axis/short axis) than those previously described (section 4.3.2). For example, nanowire lablled 1 (Fig. 5-16) has short axis a=15 nm and long axis b=586 nm. These sizes result in an extremely high lateral aspect ratio $c=(b/a)^{½}=6.25$, which corresponds to a wire with length 39.1 times larger than its width. From this long axis' length, and taking into account that this particular template was just processed 10 min in Ar-H_2, a minimum wires in-plane growth speed can be estimated as ~1 nm/s.

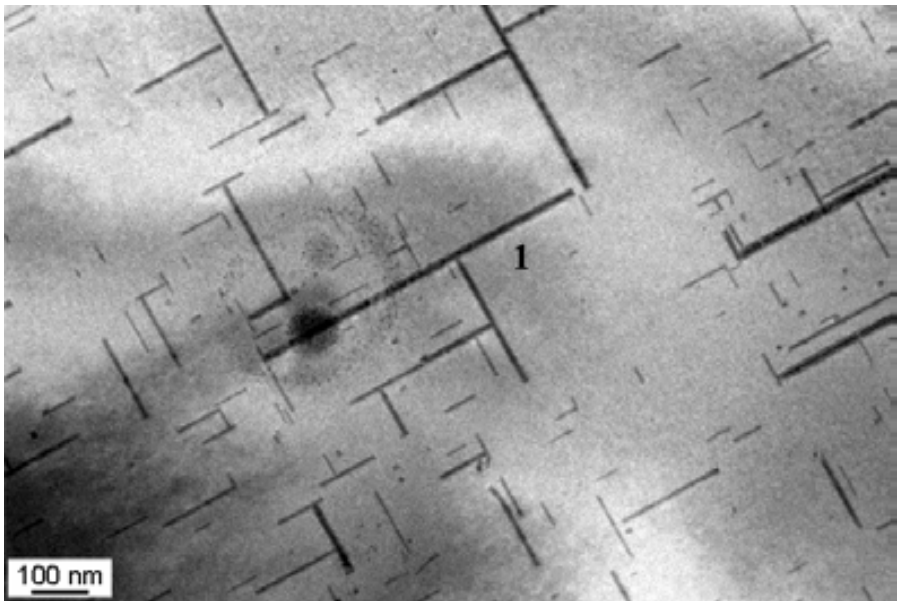

Fig. 5-16: TEM planar-view of a CGO/LAO template processed in Ar-H_2 at 1000^{o}C for 10 min. High in-plane anisotropic nanowires are observed; whereas few square-based (001)-CGO nanodots still remain after this short annealing. Wire labelled 1 has short axis a=15 nm and long axis b=586 nm, i.e. its long axis is 39.1 times larger than its width.

A great dispersion of wires' sizes is observed in this TEM planar-view (Fig. 5-16). Whereas there exists a large variety of long axis lengths ranging from 40 to 600 nm, there is a narrow size distribution of short axis widths. Even longest wires do not exhibit in any case a short axis wider than 80 nm. A correlation between height and width has already been established. Moreover, a link between island's effective diameter $D=(ab)^{½}$ and lateral aspect ratio $c=(b/a)^{½}$ can also be determined. Fig. 5-17a shows the dependence of wires' in-plane anisotropy c with its size D; experimental data is extracted from TEM planar-views images. As island's base area increases, also does its lateral aspect ratio. Thus, there is a continuous tendency to lengthen which seems to not happen at random but coupled with each island size. Fig. 5-17b shows an equivalent plot but in this case wires' dimensions were obtained from AFM topographic images. The same increasing c(D) tendency is observed though there is a displacement of data towards larger islands' sizes D and lower aspect ratios c. It is consequence of the influence of AFM's tip convolution on short axes' width; the measurement of larger *a* values affects both $D=(ab)^{½}$ and $c=(b/a)^{½}$. Thus, in this case, we gain in statistics at expenses of lateral resolution, since the area observable with AFM is larger than with TEM. In any case, it is proved that nanowires elongate as their volume increase, and a general correspondence between each size and their lateral aspect ratio is established for all wires. Notice that the extrapolation of c(D) values (Fig. 5-17a) does not cross c=1 at D=0, suggesting that (011)-nanoislands are elongated since nucleation.

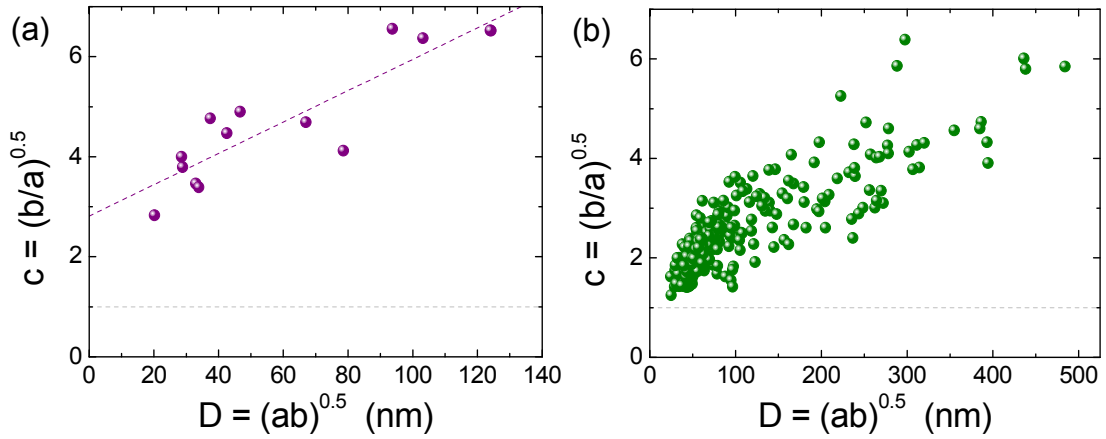

Fig. 5-17: Lateral aspect ratio $c=(b/a)^{½}$ as function of effective diameter $D=(ab)^{½}$ of (011)CGO wires: data measured from TEM planar-views (a) and AFM topographic images (b). Grey dashed line indicates the aspect ratio of an isomorphic island, i.e. c=1. Differences in c and D values displayed in (a) and (b) arise from influence of tip convolution effect in data extracted from AFM images.

Moreover, in TEM planar-view image displayed in Fig. 5-16 it is observed a constant tendency of wires to join. Impingement between nanowires mainly happens through their orthogonal axes. Particularly, 65% of the elongated islands are coupled to at least another wire perpendicularly in-plane oriented. Labyrinth-like nanostructures constituted after the junction of more than 10 orthogonal nanowires in just 10 min of heat treatment are frequently observed.

These distributions of nanowires suggest the existence of an attractive interaction between perpendicular wires. In addition to (011)-nanowires, few isolated isomorphic nanodots are also observed in this image, indicating that in Ar-H_2 at 1000^{o}C some (100) crystallites also nucleate. At this evolution stage, isomorphic dots represent less than 10% of the total number of interfacial CGO nanoislands observed; and, due to their reduced dimensions in comparison with wires, they represent an even smaller percentage of the total deposited volume and occupied substrate surface. Further attention is given to nanoislands' junction in next section 5.2.2.1, where kinetics and island's reconstruction are analyzed in detail.

To summarize, CGO nanowires are (011)-oriented and grow in a biaxial anisotropic stressed media. Their long axes align along CGO[0-11]||LAO[010], enlarging lateral facets of lower surface energy, i.e. (111), and lengthen along lowest misfit direction. Epitaxial growth is also achieved along CGO[100]||LAO[100] despite the high misfit between both structures in this direction; higher energy planes (001) limit the end of these short axes. A transition from sharp to truncate nanowires' top seems to occur as their size increase. All together results in a very singular system, where a particular trade-off between distinct energy contribution (elastic relaxation, surface and interaction energy) leads to a complex picture where no end for elongation seems to exist.

The mechanism that leads to the preferential nucleation of (011) orientation instead of (001) is unknown at present. It has been reported that small deviations from the optimal growth temperature can rapidly lead to the nucleation of orientations other than (001) for CeO_2 vacuum deposited on Ni{100} [253], where it was also proved that growth atmosphere might be another important factor. This particular crystallographic orientation has also been observed as a minor orientation in vacuum growth CeO_2 films on (001)STO [254-256]. Additionally, STO films grown on (001)CeO_2 films might also show this unusual interface [257]. For CGO thin films grown in reducing atmosphere on LAO perovskite single-crystals we did not achieve an exclusive (001)CGO epitaxial growth either. (011)-crystallites were detected by XRD[2] measurements in nearly 80% of the volume of CGO/LAO thin films processed in Ar-H_2, whereas the rest of the film essentially corresponded to (001) grains and to a nearly negligible proportion of (111)CGO (see section 4.3.3).

Thus, all these results suggest that the growth of the fluorite CGO on substrates with different crystallographic structure must be very sensitive to growth conditions. As mentioned beforehand, (001) surface of the fluorite structure has high surface energy and it is unstable due to its polar character. Consequently, nanostructures and thin films show a tendency to stabilize the facets of lower surface energy (111) and (110) when annealed at high temperatures [182, 183, 195]. We have found very particular growth conditions which promotes

(011)CGO||(001)LAO interface, whereas in another growth conditions we can achieve (001)CGO||(001)LAO as the predominant nucleated crystallographic orientation. Additionally to the isomorphic (001)-dots and elongated (011)-wires, very rarely triangle-shaped (111)CGO nanoislands have also been observed. An example is shown in TEM planar-view in Fig. 5-18; this sample was processed in Ar-H_2 at 1000^{o}C for 10 minutes. Scarce population of (111)CGO nanoislands is in agreement with XRD[2] analysis of CGO/LAO thin films, where nearly negligible proportion of (111) grains was detected. We will discuss again the nucleation of (001) and (011) CGO crystallographic orientations in section 5.3.

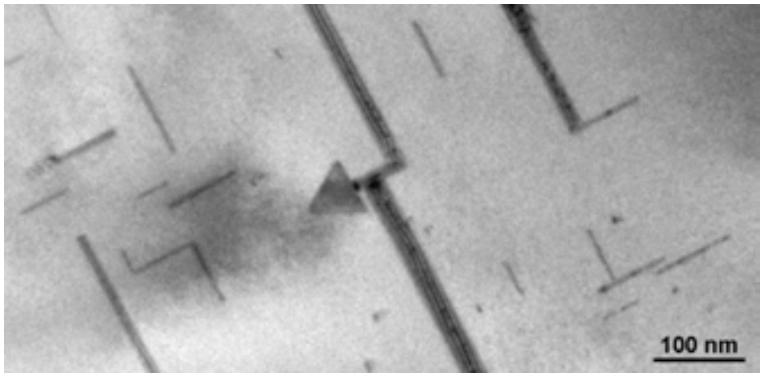

Fig. 5-18: TEM planar-view image where, in addition to (011)-nanowires and few (001)-dots, a (111) triangle-shaped nanoisland is also observed. This template was processed 10 min at 1000^{o}C in reducing atmosphere.

Nonetheless, despite we do not know the exact driving force leading to the nucleation of (011)CGO crystallites, it becomes evident that this particular crystallographic orientation arises as one of the key points for the observed differences between nanodots and nanowires, that is to say between (001) and (011) CGO nanoislands. In these first two sections, we have just suggested from experimental arguments that surface and elastic relaxation energies involved in those configurations might be different. Thermodynamic analyses are required to know if the observed shapes effectively derive from the particular energy of these islands; these studies will be presented in next chapter.

5.2 Nucleation, growth and ripening processes of CGO nanoislands

Complete understanding of interfacial nanostructures nucleation, growth and ripening implies both kinetic and thermodynamic events. Examples of kinetic parameters are atom's diffusion coefficient, anisotropy in atom's diffusion, etc. On the other hand, examples of thermodynamic parameters include surface, interfacial and elastic relaxation energies. Distinction between both kinds of phenomena is not normally straightforward, as they can be strongly linked or because their dominance and performance may change depending on work

parameter region or on the stage of evolution. Working with chemical solution deposition, despite implying some initial complex growth pathway when organic removal occurs, we are dealing with a closed system, where the total amount of deposited material is preserved during annealing. So, kinetics evolution of nanostructures is expected to lead towards thermodynamic equilibrium [15].

In just one shot after 15 min of annealing at high temperature (Fig. 5-1), it was already demonstrated in previous section that growth mechanisms lead to different nanostructures depending on the atmosphere. Nevertheless, it is a priori difficult to distinguish between thermodynamic and kinetically leaded processes. For a better understanding of the system, a detailed study of CGO nanostructures evolution on LAO substrates as function of annealing time is carried out. In next section, we investigate the distinct evolution followed by (001)-dots and (011)-wires in the same atmosphere used for their nucleation. In addition, a further detailed study of the evolution path in Ar-H_2 of a specific group of islands is also performed in order to understand the mechanisms driving islands' evolution in this atmosphere.

As observed in previous chapter, temperature plays an important role in nanostructures formation. Particularly, 1000^{o}C resulted to be the optimum annealing temperature to easily appreciate island morphological differences arising due to distinct oxygen pressure during thermal treatments. Thus, the following experiments were performed at this temperature. However, in next section, the influence of temperature on the ultrafast kinetics experienced by islands processed in Ar-H_2 is also investigated.

5.2.1 CGO nanostructures grown in oxidizing atmosphere

Let's initially start studying the evolution in O_2 ($P(O_2)$=1 bar) of nanoislands nucleated in this oxidizing atmosphere, i.e. (001)-dots. Experiments were performed using metal-organic precursor solutions within the range 0.005 - 0.008 M and under an oxygen flux of ~0.03 l/min. Under these conditions, well-defined CGO (001)-nanodots are already formed after 15 min of thermal treatment (Fig. 5-19a), though their precise size is difficult to determine within AFM resolution limits. A rough estimation indicates that their equivalent diameter and height is ~(33±12) nm and ~(6.8±2.1) nm, respectively; however, they are probably much smaller. They appear to be round; but, after TEM images we know that they are truncated pyramids with square base. Nonetheless, both shapes agree with in-plane isomorphic aspect ratio and will not alter further analysis. These nuclei are not randomly distributed; instead, a certain tendency to order in rows is already appreciated at this stage. The periodicity of nanodots' chains can be quantified performing a FFT on a wide area AFM image. In this case, separation between spots in FFT image displayed in Fig. 5-19a indicates that the mean separation between rows of nanodots is ~(93±5) nm. This distance agrees with the typical terrace width of our LAO single-

crystal substrates with miscut angle θ ~(0.23±0.01)°. Thus, these results already suggest a role of vicinal substrates as templates for nanodots self-organization.

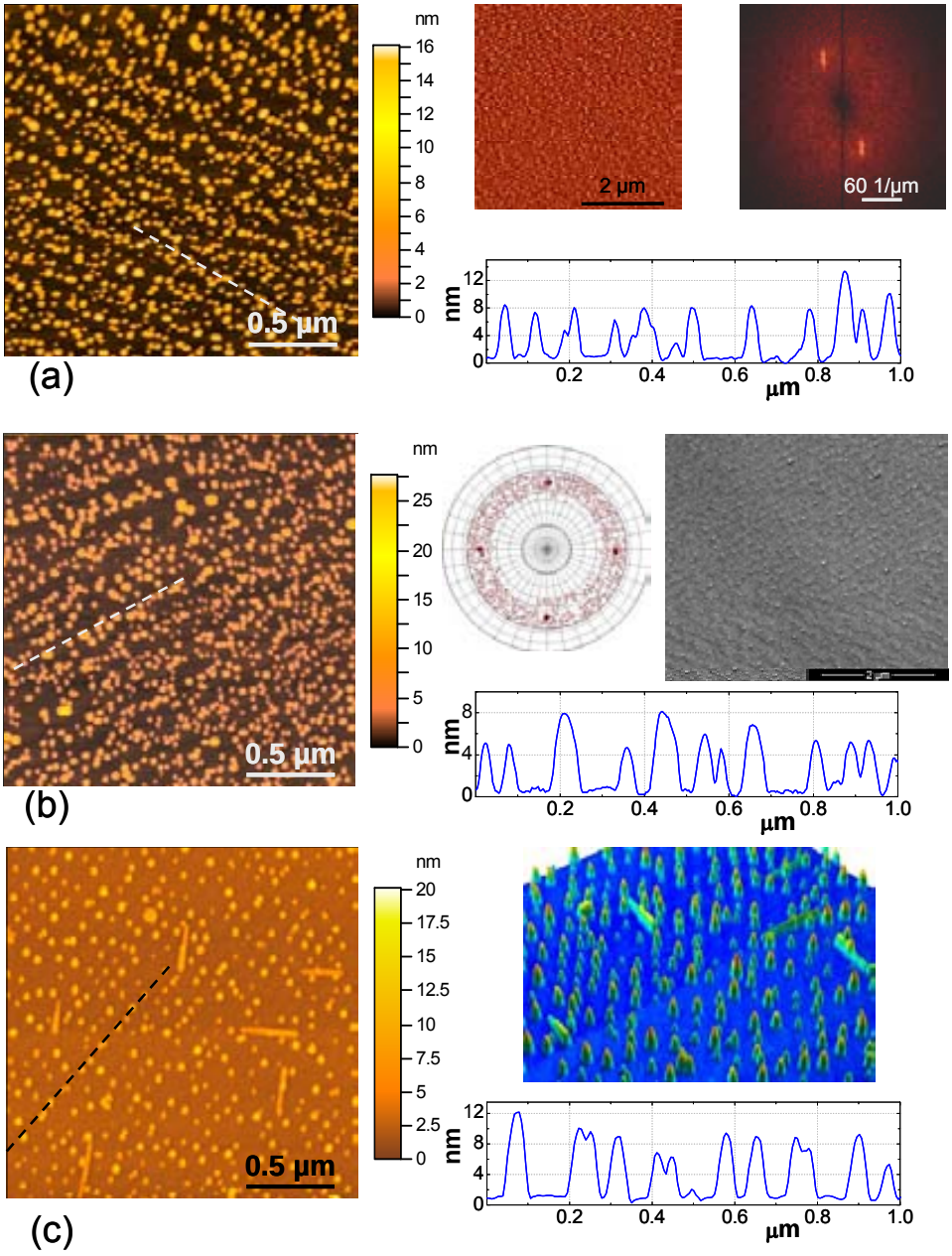

Fig. 5-19: Evolution of CGO nanoislands on LAO in oxidizing atmosphere at 1000°C. AFM images correspond to thermal annealings of 15 min (a), 30 min (b) and 8 hours (c). Typical profiles are shown for each case; additionally FFT (a) and (111)-CGO pole figure and SEM image (b) are also displayed.

Nanodots' distribution in chains along substrate terraces is preserved after longer heat treatments (Fig. 5-19b, 30 min). During these subsequent annealings, nanodots' size slightly increases at expenses of density decrease. Since we are dealing with a closed system and taking into account that the whole amorphous oxide layer formed after organic removal had already crystallized into nanoislands (as it was confirmed by the clear observation of vicinal substrate steps underneath), coarsening processes must be the mechanism leading nanodots' growth.

XRD[2] measurements proved the (001) orientation of these nanoislands, i.e. (001)CGO[110]||(001)LAO[100] as expected after results of previous section. Thus, morphological characteristics of these dots (lateral facets, shape, etc.) agree with features described in last section 5.1.1.

The achievement of high degree of self-organization of (001)CGO nanodots into rows periodically distributed on LAO substrate can be well appreciated in template shown in Fig. 5-19c. It corresponds to a sample processed in oxidizing atmosphere for 8 hours. These nanodots show a narrow size distribution with mean diameter ~50 nm (determined from AFM images) and FWHM of the Gaussian size distribution of ~24 nm, as it is observed in the histogram reported in Fig. 5-20b. Their uniformity in height is also very high, with mean value ~(7±3) nm. This homogeneity in dots' sizes indicates that self-assembling mechanisms typically observed in vacuum deposition methodologies apply effectively to CSD-grown interfacial oxide nanostructures, as it was already observed to happen in BZO-dots grown on STO by CSD (chapter 4). The clear observation of substrate terraces under nanodots evidences a Volmer-Weber-like mechanism of growth, i.e. direct growth of nanodots on a bare substrate.

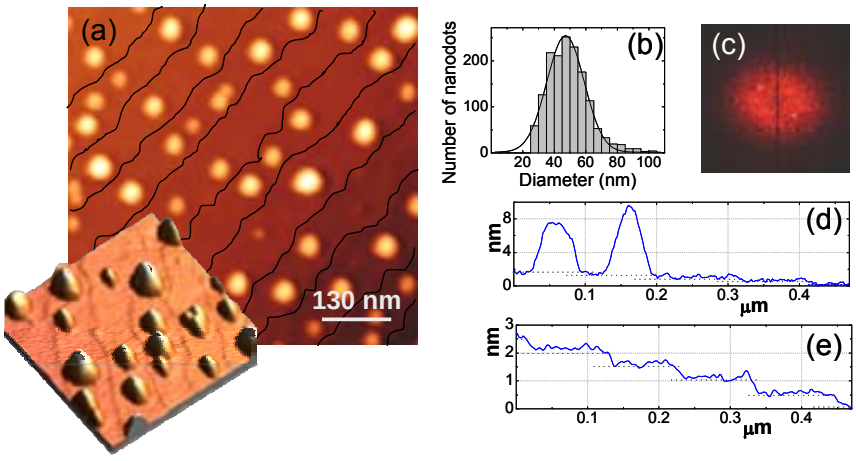

Fig. 5-20: Self-assembled CGO nanodots on LAO substrate: 2D and 3D AFM images where lattice steps are observed simultaneously with nanodots centred in substrate terraces (a); diameter distribution of CGO nanodots in this template (b); FFT ranging from -6x10^5 cm^{-1} to 6x10^5 cm^{-1} of an AFM image, where the two peaks indicates the periodicity of islands' rows (c); line scans along the substrate steps visualizing nanodots and the background, (d) and (e) respectively.

At this stage, it is found that terraces' width of vicinal substrate acts as boundary for the growth of nanodots' diameter and just very few exceptions of islands crossing lattice steps are detected (Fig. 5-19c). In fact, a closer examination confirms that underlying steps not only limit in-plane islands' growth, but they are effectively responsible for inducing the self-organization of (001)-dots in rows. In Fig. 5-20a both steps and dots are simultaneously visualized in 3D and 2D AFM images; in the latter, steps are stressed to better see their localization. Periodicity is

also verified by the two peaks in FFT displayed in Fig. 5-20c. It indicates a mean row separation of ~90 nm, which corresponds to a miscut angle θ~0.24°.

Particularly, there is a preferential and nearly total localization of CGO nanodots in the central part of the terraces, avoiding either the upper or bottom side of substrate steps (Fig. 5-20a). Actually, this is the key and most outstanding feature of these self-organized templates: *(001)CGO dots are strongly confined within terraces of LAO substrate even though their height is about ~20 times higher than lattice steps themselves* [258]. The mechanism that leads to this very unique phenomenon of confinement can only be understood through the existence of a strong repulsion between CGO nanodots and lattice steps. Line scans perpendicular to lattice steps reported in Fig. 5-20d and e stresses the mentioned height difference; the former including and the latter avoiding interfacial nanoislands. It must be noticed that vertical scales of both profiles are remarkably different.

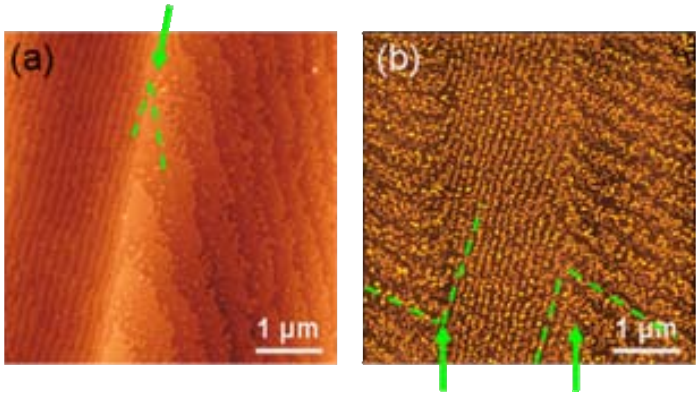

Fig. 5-21: AFM topographic images displaying unit-cell steps and twin boundaries in LAO substrate without (a) and with (b) (001)CGO nanodots grown on top. The localization of CGO nanodots directed by LAO substrate steps is clearly appreciated. Arrows indicate the twin boundaries.

The power of lattice steps as confining barriers for CGO nanodots and driving force for their organization is unquestionable appreciated in Fig. 5-21. Due to phase transition between cubic symmetry typical at high temperatures and rhomboedral one at low temperatures, LAO substrates are characterized by the formation of rhomboedral crystallographic domains separated by twin boundaries when they are cooled below T_c~500°C [175] (see also section 3.1.4). As a result of this feature and because the single-crystal polishing is performed at room temperature, some non flat facets are formed. High temperature growth is therefore performed on terraces which change the width and orientation at each twin boundary, as displayed in Fig. 5-21a. CGO nanodots' localization is found to be highly dependent on LAO steps' orientation and distribution (Fig. 5-21b): separation between chains of nanodots as well as rows' orientation drastically changes at twin boundaries (which are signalled by arrows in the figure).

Particularly, in one side of the twin boundary dots' rows are separated ~(360±30) nm, whereas in the other there is a mean separation of ~(125±8) nm. Both distances agree with underneath lattice steps periodicities, which would correspond to "equivalent" miscut angles of 0.06^{o} and 0.17^{o}, respectively. Consequently, Fig. 5-21 confirms the extremely high efficiency of lattice steps as a confining template for (001)CGO nanodots.

Calculations based on the medium volume and mean separation of dots distributed in each substrate terrace indicate that similar CGO nanodots' total volumes are localized within each terrace, at least for the investigated evolution stages. So, atomic diffusion across steps might be negligible and, consequently, previously described coarsening processes are confined to each single terrace. Hence, it seems that some kind of barrier is acting at lattice steps. As mentioned in previous chapter (section 4.2.4), 2D thin film growth on vicinal substrates is usually influenced by Ehrlich-Schwoebel barrier [58], which reduces atomic diffusion across substrate steps. We must wonder why the present step barrier bears such an extraordinary effectiveness, i.e. ability to confine nanostructures ~20 times higher than the step-barrier itself. In heteroepitaxial growth of 2D systems by vacuum deposition, the diffusion length of the adatoms with respect to terrace width controls the dimensionality and morphology of nanostructures. At low coverage, nanowires or strings may form through step flow phenomenon, being attached either at step's top or bottom depending on the balance between "vertical" interfacial energy at steps and strain relaxation at the edges [89, 200, 216, 217, 259, 260]. For 3D systems, the situation becomes more complicate although "vertical" interfacial energy usually plays a minor role. For oxide BZO/STO system we have already proved (chapter 4) that steps act as attractive sites for BZO nanodots localization, where strain relaxation could be higher in a way similar to semiconducting quantum dots placed in order by using previously lithographed templates [218]. But, for the (001)CGO||(001)LAO system a high "vertical" interfacial energy seems to arise probably as a consequence of the crystalline dissimilarity between fluorite CGO and perovskite LAO. It might turn steps into strongly repulsive sites. At step edges, interfaces between {110}-CGO planes and {100}-LAO planes should occur if the miscut direction of the crystal is along {100}; when the miscut direction occurs along non-specific directions the interface will correspond to high index (hkl) planes. In both cases, these configurations must be of high interfacial energy and the system tries to avoid them. Therefore, the key factor promoting self-organization in the present heteroepitaxial system is the existence of an extraordinary confining efficiency of dots on lattice steps due to the crystalline dissimilarity between fluorite and perovskite structures, which leads to high interfacial energies at steps [258].

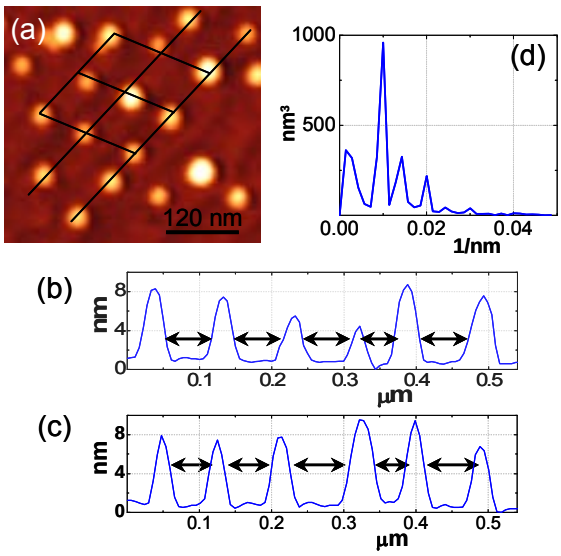

Fig. 5-22: Tendency to local 2D-order of (001)CGO nanodots on LAO substrates: AFM topographic image, where square lattice is drawn indicating local 2D order (a); line scans along (b) and perpendicular (c) to the substrate terraces, where similar separation between nanodots is indicated; power spectrum proving periodic separation between nanodots confined in a single terrace (d).

Coming back to CGO nanodots within the same terrace, a regular interdot separation is sometimes detected. Besides visual observation (Fig. 5-22a), power spectrum analysis also corroborates it (Fig. 5-22d). Power spectrum S(**K**) is a powerful tool based on reciprocal space analysis displaying information of the strength of variations present in a series of data. Computing power spectrum density is done by the FFT method; actually most software devoted image processing incorporates this option. Applying it to an AFM image, it corresponds to $S(\mathbf{K})=[F\{z_{ij}\}]^2$ where F is the Fourier transform and z_{ij} is the function which associates each (x_i, x_j) point a height $z(x_i, x_j)$ [13]. As a result, for example, it allows to quantify the separation of structures of a pattern formation. When applied to a profile of nanodots distributed in a single terrace (Fig. 5-22b), one obtains an array of distinct peaks, as shown in Fig. 5-22d. The location of the first peak in the reciprocal space yields to the medium separation between dots. The peaks broaden and decrease indicating a non-perfect order. In this case, it is found that average separation between dots residing in a terrace is ~95 nm, value very close to our typical LAO substrate terrace widths and, thus, to rows' separation. Hence, it indicates that a tendency towards 2D self-organization is locally achieved. Notice that similar internanodot distances are observed in line scans along and perpendicular to substrate's terraces in Fig. 5-22b and c, respectively. Nanodots' periodicity along terraces suggests that self-organization processes based on long-range strain-induced repulsive interaction mediated by the substrate might be effective for nanodots residing in a single terrace [15, 46]. In Fig. 5-22a, a square array has been drawn on top of the AFM image to notice this local 2D order. For systems with cubic anisotropy of the elastic medium and islands with square base, the balance of energies was proved to result

in a square lattice arrangement of islands as the most favourable configuration [15]. Since our system satisfies both conditions, the local 2D self-ordered observed could be attributed to a minimization of repulsive interaction energy between dots boosted by lattice steps. Note, however, that the crystallographic orientation of the terraces does not correspond, in general, to a "soft" main crystallographic axis of LAO. The degree of self-organization of the dots along the terraces could be enhanced, therefore, if they were oriented along some of these softer crystallographic directions.

So, despite the formation of very few elongated structures, most of the deposited material still remains within small nanodots of narrow size distribution after 8 hours annealing in O_2. Therefore, (001)-nanodots grown in oxidizing atmosphere display limited coarsening processes. By presenting (111) lateral facets, system is probably adopting the configuration of lowest surface energy and, so, there is no need to minimize the total area of the islands through increase of island's volume. Moreover, being orientated (001)CGO[110]||(001)LAO[100], the island is in the lowest lattice mismatch configuration; and, consequently, it minimize as well its strain energy. Nonetheless, both energetic contributions must be simultaneous considered to accurately establish dots' equilibrium shape. Hence, in thermodynamic analysis introduced in chapter 6 the coarsening tendencies of this system will be investigated in detail taking into account elastic relaxation and surface energy.

Recalling the large structures observed in Fig. 5-19c, their formation can be attributed to a distinct crystallographic orientation, which may show different equilibrium shape and experience differentiated kinetics. X-ray studies on CGO/LAO thin films pointed out that in general a unique epitaxy was not achieved in oxidizing atmosphere (section 4.3.3.): although (001) was the major population, some few (111) or (011) crystallites were also present (see also end of section 5.1.2). This must be the case of the few nanoislands in Fig. 5-19c which are not confined within substrate steps and which show strong resemblance with (011)-elongated structures.

5.2.2 CGO nanostructures grown in reducing atmosphere

The general evolution path followed by interfacial CGO nanostructures grown on LAO single-crystals in Ar-H_2 reducing atmosphere is displayed in Fig. 5-23; whereas a detailed study of the evolution of few specific nanoislands is presented later. All the following experiments were performed at 1000^{o}C during heat treatments ranging from 5 min to 8 hours; and Ar-H_2 flux was kept within the range 0.012-0.03 l/min. Metal-organic precursor solutions of 0.008 M were used.

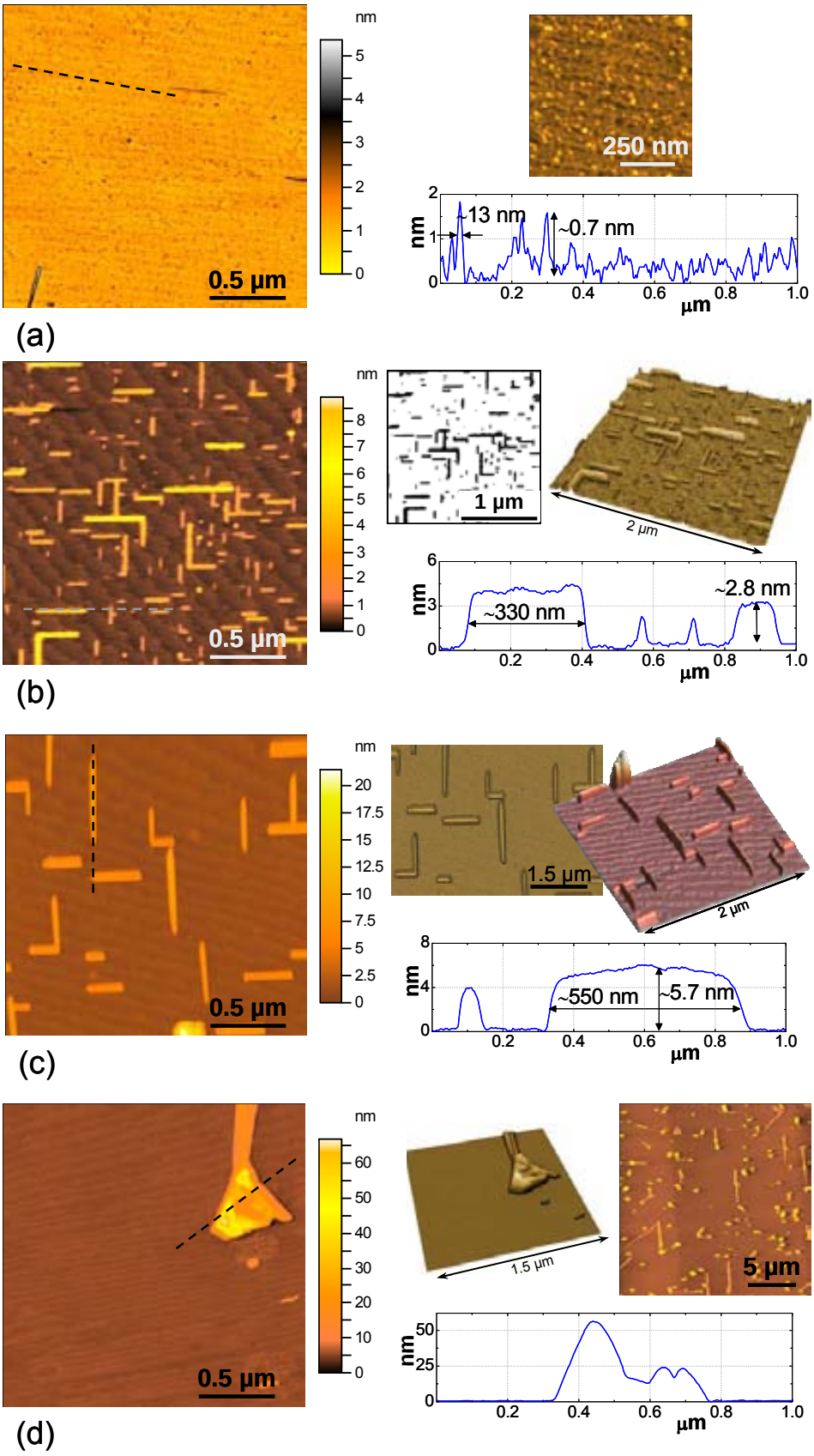

Fig. 5-23: Sequence of AFM images showing the evolution of CGO nanoislands on LAO substrates in Ar-H_2 at 1000°C as function of annealing time: 5 min (a), 10 min (b), 30 min (c) and 8 hours (d). Characteristic profiles and 3D AFM views are also displayed. All samples were prepared from 0.008 M precursor solutions.

Just upon 5 min of thermal treatment (Fig. 5-23a), the formation of first stable nuclei is already distinguished. They are 0.7-0.9 nm in height, which corresponds to just two fluorite unit-cells; and their diameter lays in the range of (13±5) nm, dimensions that can be appreciate in profile shown in the same figure. These nuclei emerge from a disordered background with peak-to-valley heights ~0.5 nm, where they appear sparsely distributed suggesting a random nucleation with density of ~190 nanoislands/μm^2. Therefore, CGO nuclei formation in reducing atmosphere also follows a modified Volmer-Weber mechanism, where nanodots merge from the uniformly distribute quasi amorphous layer formed after metal-organic decomposition of precursor solutions. Due to the small size of nanoislands and because of AFM resolution limits, the degree of anisotropy of these first nuclei cannot be established. Nonetheless, it is worth to notice that some few nanowires of ~380 nm length and ~1.1 nm height are already formed during this very short annealing period.

The in-plane anisotropic character of most interfacial CGO nanoislands becomes definitely evident after 10 minutes of thermal treatment (Fig. 5-23b); landscape of CGO nanostructures grown in reducing atmosphere is drastically modified in just five minutes of annealing (interval time between Fig. 5-23a and b). By then, most of the deposited material is constituting nanowires, though few isomorphic (001)-nanoislands are still observed. Therefore, it evidences, again, the incredibly high atomic diffusion which facilitates the formation of highly elongated structures after the ripening of previously observed nuclei and incorporation of material coming from the background amorphous layer. At this stage, the formation of 3D islands is complete in the sense that no amorphous material remains in the background, as confirmed by the clear observation of substrate steps underneath. Small nanowires try to remain within terrace limits, suggesting that confining mechanisms observed for (001)-dots also apply to these wires' sizes. As nanowires elongate, they end up crossing substrate steps and they are not confined any more. Long wires can extend over several lattice steps. Therefore, despite vertical interface energies at step edges are initially effective, nanowires are finally able to surmount these energy barriers, probably leading the system to a lower configuration energy achieved thanks to nanowires' elongation.

XRD[2] confirmed the (011)CGO||(001)LAO orientation of these elongated nanostructures. Again, the apparition of 4 peaks at $\chi \sim 35^o$ in the (111)-CGO pole figure explains the existence of two in-plane populations of nanowires orthogonally orientated as a consequence of the two-fold symmetry of this orientation.

In AFM image displayed in Fig. 5-23b and specially in the corresponding digitalized picture, it is again observed that nanowires very often join through their orthogonal axes into dimers, trimers or even higher order clusters keeping a nice mutual orthogonal distribution, which leads to very intricate nanolabyrinthine structures. A remarkable tendency of nanowires to join orthogonally through their short axes in 90^o configuration is specially distinguished.

When different nanowires meet, they quickly reconstruct into a larger one, as shown in the advanced evolution stage displayed in Fig. 5-23c, where wires mean size is larger than those seen in Fig. 5-23b, and consequently, islands' density is lower. In this case, template remained in the furnace for 30 min.

The formation and distribution of nanowires is homogeneous all over the 5x5 mm^2 substrate. However, the proportion of (001)-dots with respect (011)-wires as well as the length of wires might slightly change from zone to zone. Fig. 5-24 shows two large area images taken with Field Emission Scanning Electron Microscope (FESEM); they correspond to two distinct regions of a same CGO/LAO template separated ~2 mm. So, the capability of CSD to generate homogeneous nanostructured oxide templates is proved.

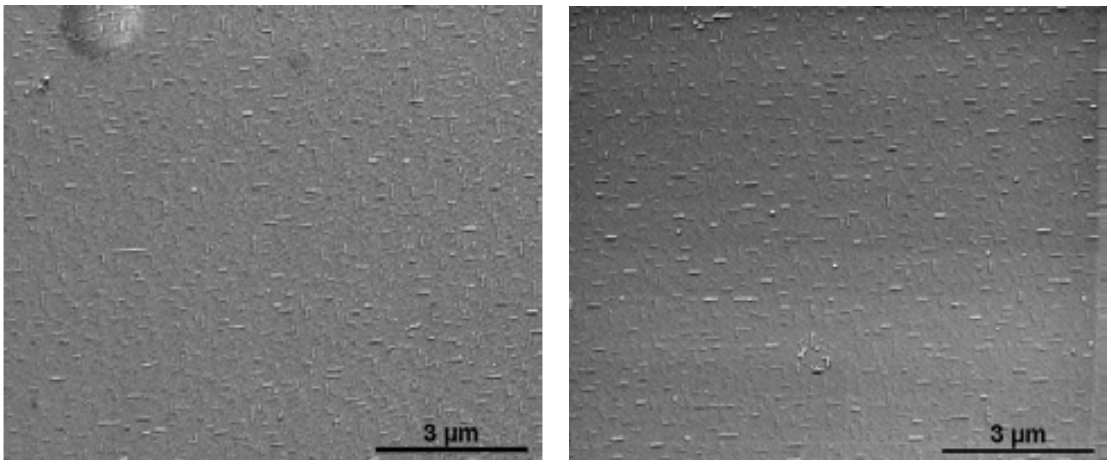

Fig. 5-24: FESEM images of two distinct regions separated ~2 mm of the same CGO/LAO template processed in Ar-H_2 at 1000°C during 30 min; 0.008 M precursor solution was used.

These larger nanowires are not stable structures neither. Indeed, highly complex polyhedral structures form after much longer annealings. After 8 hours of heat treatment, nanostructures are about ~(60±20) nm in height and ~(470±170) in equivalent diameter, and there are less than 0.3 nanoislands/μm^2. That is the case of template shown in Fig. 5-23d. Other examples of this advanced evolution stage are observed in FESEM images displayed in Fig. 5-25. It is worth to notice the scale bar of these images compared to those typical displayed in AFM images. These nanostructures' large sizes indicate that ripening seems to have no end. Although island shape is modified, coalescence does not stop. In fact, disappearance of wires could be consequence of their own tendency to infinitely elongate. In general, atoms incorporated to the receiving (011)-nanowire might diffuse till its extremes to construct a longer island. It has been proved in previous sections that lateral growth occurs much faster than vertical growth and, in particular, long axis rapidly elongates whereas wires' width remains fairly constant. Hence, it is possible that nanowires reach a length at which present kinetic mechanisms are not effectively any more to maintain the continuous elongation of the islands. For example, that would be the case when the frequency of arriving atoms is higher than the

time required to diffuse them till islands' ends and, thus, there is not time enough to reconstruct the longer wire. As a result, the whole wire might collapse. Then, large polyhedral structures may form instead of wires with larger lateral aspect ratios as consequence of kinetic limitations for such islands' volumes and under the present growth conditions.

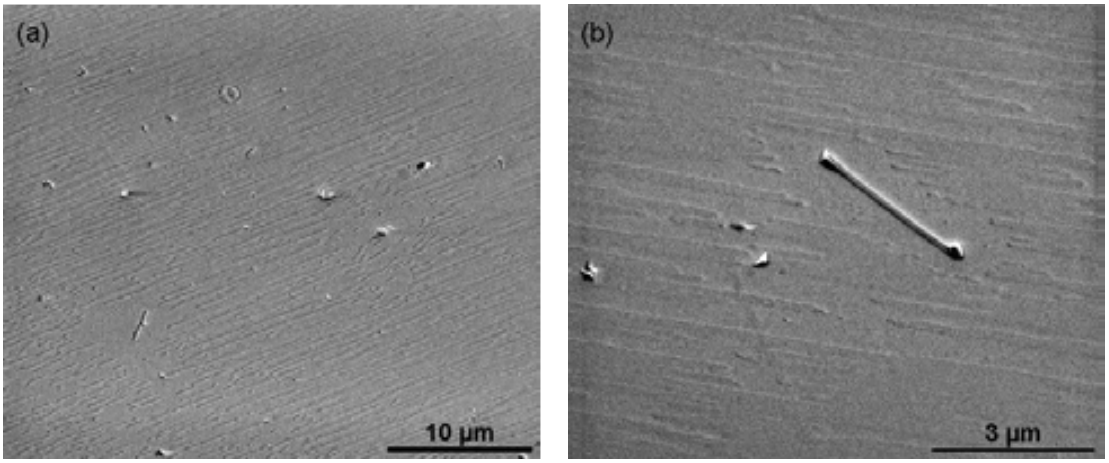

Fig. 5-25: FESEM images of a CGO/LAO template annealed 8 h at 1000°C in reducing atmosphere; 0.008 M precursor solution was used. Notice the scale bar in comparison to typically displayed AFM images.

Through the distinct snapshots showed above, we have given a general overview over the whole life of interfacial (011)CGO nanoislands in reducing atmosphere, from born to dead. That is: nucleation, growth, ripening and collapse of wires. Most changes happen essentially during first hour annealing; thus, a great variety of phenomena must be taking place simultaneously in order to explain such an extraordinary effective mobility. Sequence displayed in Fig. 5-23 is too general if one tries to discern the exact steps followed by wires during their evolution. Therefore, localization and study of a specific group of islands is required to accurately determine the processes involved. Due to the richness and diversity of the present system, next subsection is entirely deserved to this objective.

5.2.2.1 Coalescence phenomena of (011)CGO nanoislands in reducing atmosphere

Since most processes involving CGO-nanostructures evolution in Ar-H_2 take place in very short periods of time (often of the order of minutes) and because reiterate localization of a particular group of islands with typical AFM procedure is not possible, a specific experiment was designed. Short annealings of just 5 minutes followed by AFM imaging was the process repeated time after time. For unambiguous localization of the same area in the template, nanoindentation marks were made on the substrate (prior to deposition), which resulted into plastic deformation of the substrate (Fig. 5-26). These marks were big enough to be seen through the optical microscope coupled to the AFM; and then, once AFM tip was situated there, we took advantage of AFM moving stage to always find the same group of islands. As a result,

sequences like the one displayed in Fig. 5-27 were obtained. Different snapshots correspond to annealing times of 15 min (a), 25 min (b) and 40 min (c), respectively, at 1000^{o}C in Ar-H_2. Wires' labels as well as substrate steps serve as reference.

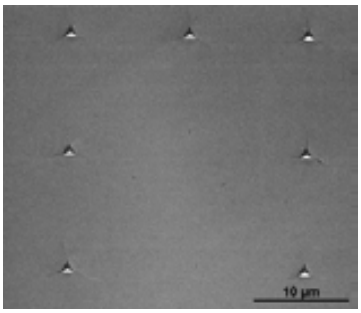

Fig. 5-26: FESEM image of nanoindentation marks on a LAO single-crystal substrate done prior to deposition, and used to localize the same area of the substrate. Consequently, evolution of a determined group of islands could be studied.

In Fig. 5-27, nanowire's elongation as function of annealing time is observed for the wire named 1. A zoomed view of its evolution and corresponding profiles are shown in Fig. 5-27d. Initially, this wire is formed though the junction of two smaller nanowires, one of ~9.8 nm high and ~110 nm long and another one with height and length of ~18.5 nm and ~120 nm, respectively. The union of these two distinct blocks is clearly seen through orange line in profile in Fig. 5-27d. The distinct height of joined blocks indicates that at this stage the wire is in state of "quasi-equilibrium". In subsequent annealings, a tendency to island reconstruction and height homogenization is observed, i.e. the wire seems to evolve towards the equilibrium shape. However, at the same time, nanoislands from the surroundings are incorporated. Height differences between distinct wire's top regions are not more than 5 nm after 10 min of additional annealing (green profile in Fig. 5-27d). Finally, the reconstruction leads to a uniform wire of ~375 nm length and ~14 nm high, with height oscillations of just ±0.8nm (Fig. 5-27d, purple line). Consequently, nanowire elongation through the coalescence of nanoislands followed by a shape reconstruction towards an equilibrium shape is proved.

In the same sequence (Fig. 5-27), reconstruction of orthogonal wires' is also observed. Group labelled 2 is initially formed by two orthogonal nanowires touching each other through their long and short axis (Fig. 5-27a). Longer wire rapidly absorbs other islands lying around, at the same time that smaller nanowire becomes shorter since their atoms diffuse to the long one (Fig. 5-27b). Then, the whole system reconstructs into a unique wire (Fig. 5-27c). Within the observed range of times (40 min), an island with homogeneous height is still not reached. Even though, a path similar to that described for wire 1 is expected to be followed. Incorporation of short nanowire into the longest one can be followed through colour profiles and zoomed views in Fig. 5-27e.

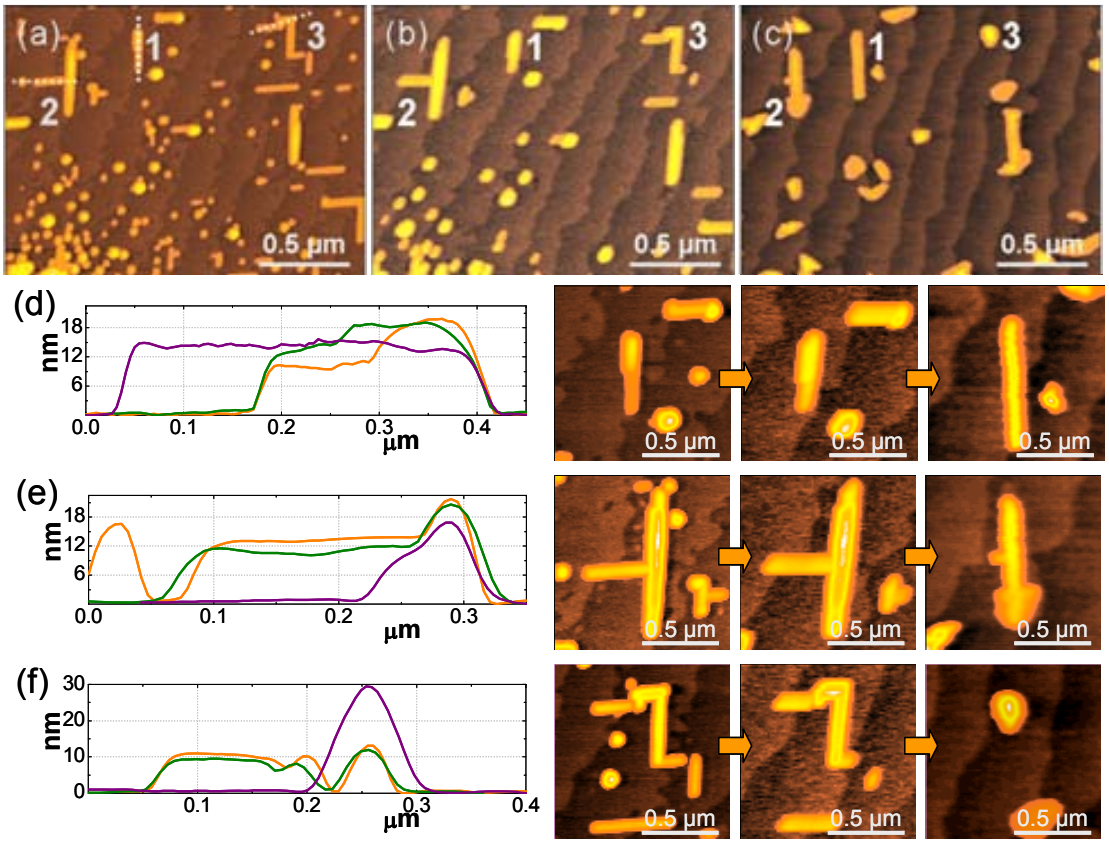

Fig. 5-27: AFM sequence displaying the evolution of specific CGO nanoislands in Ar-H_2 at 1000°C. Distinct snapshots correspond to annealings of: 15 min (a), 25 min (b) and 40 min (c). Nanowire's elongation and nanowires' junctions reconstruction can be followed through structures labelled 1, 2 and 3, whose specific profiles (indicated as dotted lines in (a)) and zoomed views at each evolution stage are shown in (d), (e) and (f), respectively. Different profiles' colour curves correspond to the distinct stages of evolution, i.e. 15 min (—), 25 min (—) and 40 min (—).

As mentioned above, in advanced evolution stages nanowires' reconstruction leads sometimes to large polyhedral structures. That is exemplified by the intricate group named 3. In the first snapshot (Fig. 5-27a), the group is constituted by the union of at least 5 orthogonal nanowires plus some isolated islands staying in the proximities, which again are soon absorbed by the labyrinthine group (Fig. 5-27b). Finally, reconstruction of the cluster leads to an only one 3D irregular island of ~117 nm in base diameter and ~30 nm in height (Fig. 5-27c). A rough observation of these processes is depicted through the transversal profiles in Fig. 5-27f; corresponding zoomed views of this evolution path are as well displayed. The structure of these large irregular polyhydral nanoislands is unknown, but it is very likely that they correspond to some kind of "instable" morphology hindered to achieve the corresponding "quasi-equilibrium" shape by kinetic limitations which become more relevant at large islands' volumes.

A tendency of lattice steps to act as barriers against diffusion is also guessed through the evolution sequence shown in Fig. 5-27. For example, main nanowire of group labelled 2 elongates along [100] substrate direction but it remains entirely confined in a single substrate

terrace; isolated nanodots are preferentially localized at the central part of substrate terraces. This confinement phenomenon seems to apply more to isomorphic nanoislands than to elongated ones, in agreement with previous results observed in section 5.2.1.

In images in Fig. 5-27, as well as in those in Fig. 5-23, the joint of (011)-nanowires is observed to take place mainly between short-long facets of different nanoislands leading to very characteristic orthogonal multinanowire clusters. It is also noticeable that a great number of nanowires join themselves perpendicularly at their ends, resulting into beautiful zigzag nanowire chains, and suggesting an attractive behaviour between them. Fig. 5-28 exhibits two more examples of clusters of nanowires joined in these distinct configurations. It is worth to note the change in height along each wire's profile, which clearly indicates the union points of different orthogonal nanowires. The exact meaning of these height anomalies is an issue worth of more detailed investigation, particularly through TEM. As it is observed in Fig. 5-14, the morphology of the nanowire is perturbed at these contact points where some mass transfer occurs, hence modifying the nanowire's height. Furthermore, junction of nanowires can also occur between wires aligned in a single direction, leading in this case to the formation of extremely long wires resulting from the union of several individual islands. One of these union points is indicated in Fig. 5-28b by the blue arrow. Coupling between nanowires' long axes is never observed, like if repulsive interaction existed between these equivalent island sides. Actually, parallel growth of (011)-nanowires separated less than 20 nm is very often observed (i.e. Fig. 5-16).

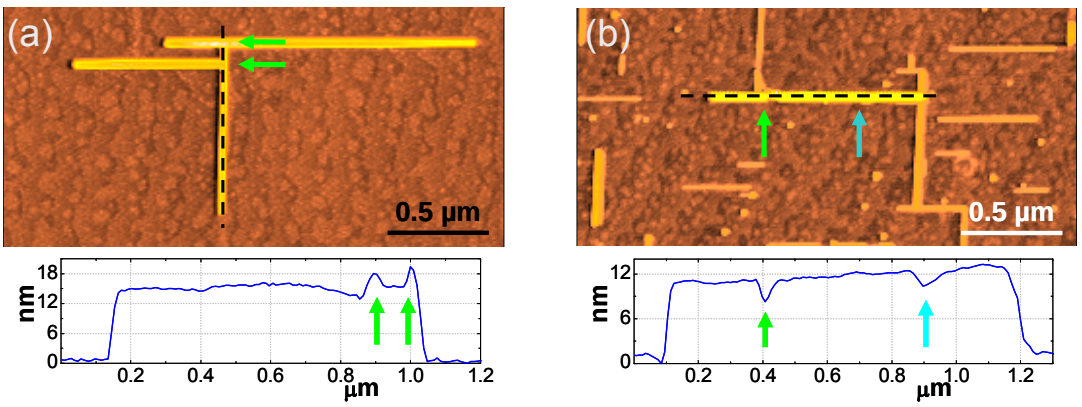

Fig. 5-28: AFM topographic images and corresponding line scans showing the joint (indicated by arrows) of several nanowires, in orthogonal configuration (green arrows) and along a single direction (blue arrow).

Such a high density of clusters with orthogonal nanowire joints seems difficult to be explained merely resulting from a random positioning of wires. Fig. 5-29 displays a topographic AFM image of a CGO/LAO template prepared using an ultradiluted precursor solution, i.e. 0.004 M, which corresponds to an equivalent thickness of just ~0.2 nm, i.e. less than one unit-

cell. Despite the lower density of islands in this template (0.04 wires/μm^2), the only two orthogonal wires present in a 42 μm^2 area have impinged through their short axes. This behaviour hints the existence of an attractive interaction between wires' ends; otherwise it seems very unlikely that the impingement of wires would occur.

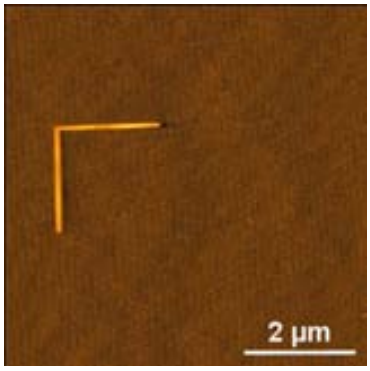

Fig. 5-29: Orthogonal impingement of the two only nanowires present in a 42 μm^2 region of a CGO/LAO template. This sample was prepared from 0.004 M precursor solution; and annealed at 1000^{o}C for 30 min in reducing atmosphere.

Fig. 5-30 displays other examples suggesting attraction between wires' axes. In Fig. 5-30a, two wires are aligned in a single direction but still not in contact; this is probably a snapshot obtained just before the joint takes place. This figure clearly suggests that some attraction happens among nanowires along this direction. In Fig. 5-30b, a snapshot image of junction of two perpendicular islands has been obtained just before this occurs.

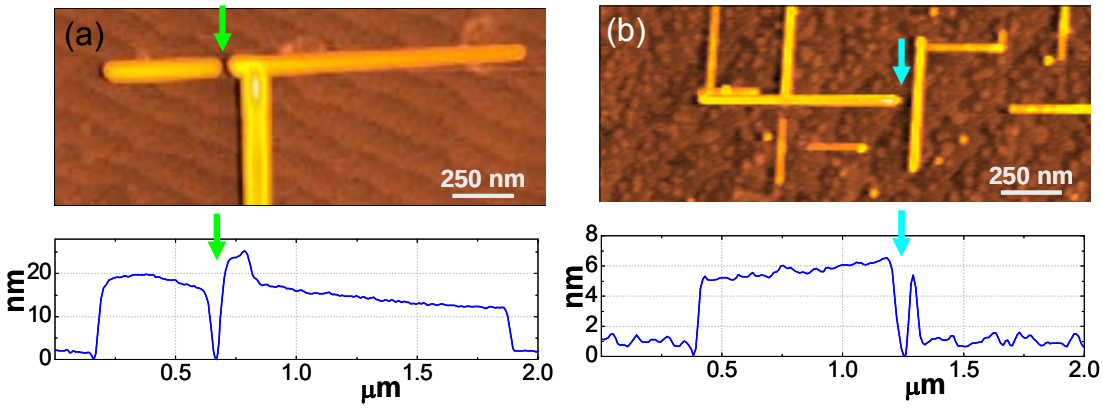

Fig. 5-30: Nanowires in process to join through their short-short (a) and short-long (b) axes. Arrows indicate the position where the junction will occur.

All examples above have shown distinct snapshots of the junction and evolution of nanowires into clusters and further reconstruction into a larger nanowire. In addition, AFM image in Fig. 5-31 displays the precise moment when the full reorganization of two nanowires happens. In this particular case, reconstruction occurs based on previous dissolution/melting of the attached nanoisland.

Fig. 5-31: AFM image in the precise moment when the reconstruction of two impinged nanowires takes place.

However, nanowires reconstruction into large structures not always implies previous touching; it can also happen through atoms migration from wire to wire. This coalescence mechanism is appreciated in Fig. 5-32, where consecutive snapshots taken exactly at the same place are presented. Islands levelled 1 and 2 as well as the dots' pile on the left side of the images serve as reference. Following the evolution path of "horizontal" nanoisland signalled with a yellow arrow, we can observe how this nanowire disappears because of atoms flux to the closer and larger "vertical" nanowire, in spite of not being physically in contact. Diffusion of atoms is distinguished to be faster for atoms closer to the host island. This behaviour could suggest the existence of localized attractive fields close to wire short axis ends associated to

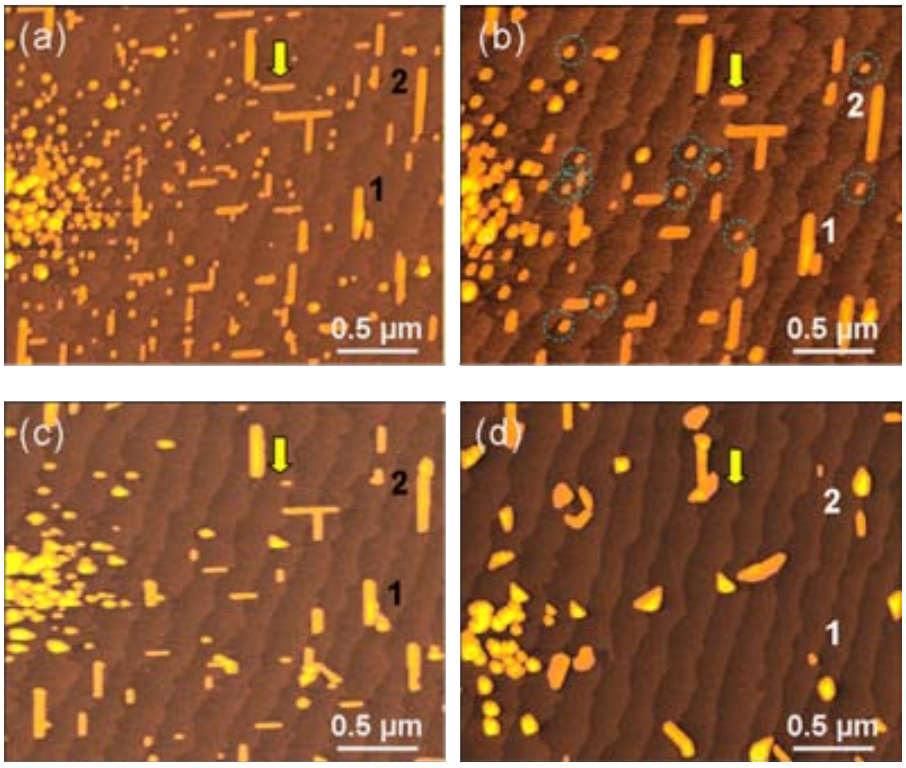

Fig. 5-32: Evolution of specific CGO nanoislands on LAO substrates in Ar-H_2 at 1000^{o}C; corresponding to annealings of 15 min (a), 25 min (b), 30 min (c) and 45 min (d). Islands labelled 1 and 2 serve as reference. Yellow arrow signal the evolution of a nanowire whose atoms migrate to another nearby wire; and blue circles (b) indicate some of the nanodots that are engulfed in next 5 min annealing (c).

strains. Therefore, conventional coarsening might be modified by the presence of strains. The incorporation of these atoms, together with others coming from other islands, leads to the reconstruction of the recipient island especially in its ends, as clearly seen in Fig. 5-32d.

An intermediate mass transport mechanism between displacement of a whole island and atomic migration can also be considered after example displayed in Fig. 5-33. Transfer of material as nanometric islands seems to take place between (011)-nanowires along [100] and [010] substrate directions; though dissolution of a previous existing nanowire towards near ones cannot be disregarded either.

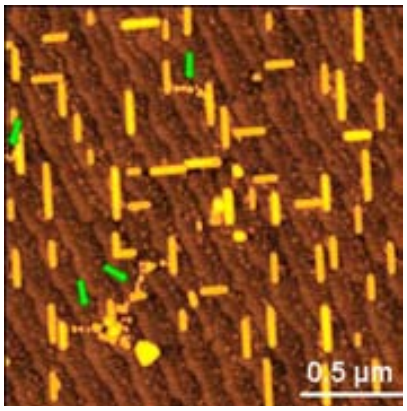

Fig. 5-33: Material transfer between CGO nanowires could explain the nanometric nanoislands of material indicated by the arrows.

In many cases, in addition to coalescence or atomic diffusion between (011)-nanoislands resulting into a larger structure, nanowires also increase their volume through the incorporation of atoms coming from (001)-islands, i.e. dots. As mentioned beforehand, a unique epitaxy (011) is not normally exclusively achieved after nucleation at 1000^{o}C in reducing atmosphere; and, in fact, some few (001)-oriented nuclei are also present at first evolution stages. Under present growth conditions, and contrary to their behaviour in templates processed in high oxygen pressure, (001) isomorphic nanoislands quickly disappear engulfed by anisotropic nanoislands, which seem to act as attractive sites. Dots' engulfment by wires is stressed in Fig. 5-32 between image (b) and (c). Most of nanodots that are absorbed have been surrounded by blue circles to easily observe them (Fig. 5-32b). Both images are just separated by 5 min annealing at 1000^{o}C in Ar-H_2 atmosphere. So, the diffusion speed under these conditions is estimated to be at least of ~0.5 nm/s, which is the maximum possible time spent by these circled nanodots to attach to the nearest larger island. Another example of the coexistence of isomorphic (001)-nanodots (i.e. square-based islands) and (011)-nanowires at first evolution stages in Ar-H_2 heat treatments is exhibited in Fig. 5-34. This TEM planar-view image corresponds to a CGO/LAO template prepared from 0.008 M precursor solution and annealed 10 min at 1000^{o}C in reducing atmosphere. Despite most nanoislands observed are anisotropic

(with short axes of ~11-30 nm width and long axes ranging from ~ 42 nm to ~ 450 nm length), few square-shaped nanoislands are as well distinguished. Notice again the remarkable tendency of nanowires to attach ones to the others.

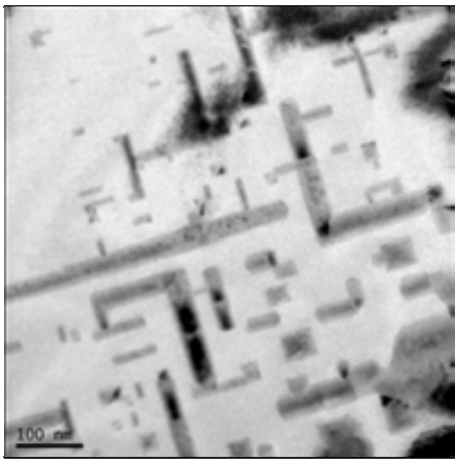

Fig. 5-34: TEM planar-view showing the coexistence of (001)-nanodots and (011)-nanowires after 10 min of heat treatment at 1000°C in reducing atmosphere. A 0.008M precursor solution was used.

As it has been pointed out for the case of nanowires, incorporation of dots' material into wires can also occur by atomic diffusion (Fig. 5-32) or by displacement of the whole dot towards the host wire. Fig. 5-35 shows a particular example of a nanowire surrounded by isomorphic nanoislands, where a tendency of dots to attach to its lateral facets is distinguished. In this case, the whole nanodot diffuses till it collides with the nanowire, instead of coarsening occurring through the diffusion of atom by atom from dot to wire. Once together, dot "dissolves" and their atoms must mainly travel till island ends, since nanowire's length was proved to continuously increase with its size whereas its width remains fairly constant.

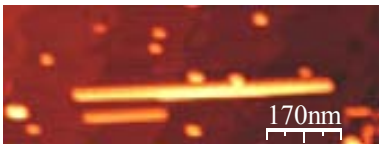

Fig. 5-35: Nanowire with dots attached in its lateral facets.

However, nanodots do not always attach to an already formed wire and atoms diffuse on it to reconstruct into a larger island. They can also take "active part" in the formation of a longer wire. Fig. 5-36 displays the simultaneous union of dots and wires resulting into a larger wire. Four nanodots of ~90 nm of lateral size are "sandwiched" between two wires of ~820 nm length resulting into a ~2 μm long island. Despite the distinct parts constituting this new wire are still clearly differentiated, they are all expected to reconstruct in a way similar to that of wire labelled 1 in Fig. 5-27, resulting into an homogenously high wire. The present situation of "quasi-equilibrium" is merely due to islands aligned in a single direction and no perpendicular

wire is present. Formation of these multiple structures aligned in a single direction also points to the existence of attraction between islands, specially when taking into account that this 2 μm-long island grow in a template prepared from an ultradiluted solution of 0.004 M, like the example displayed in Fig. 5-29.

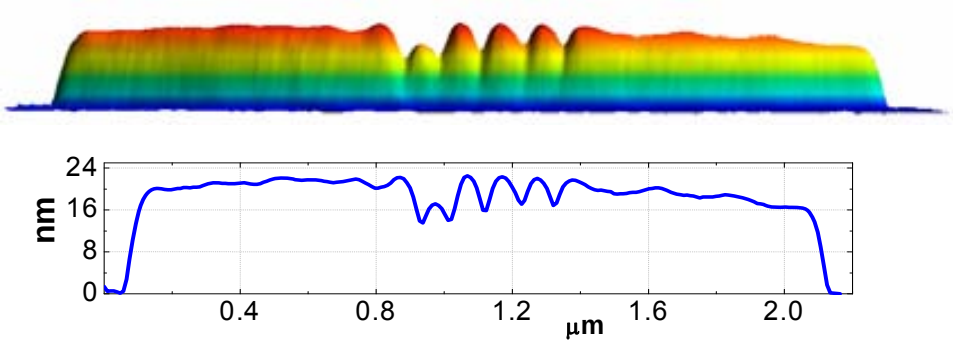

Fig. 5-36: 3D AFM image and corresponding profile of an elongated CGO island (~2 μm) formed after the union of nanowires and nanodots.

Comparing the first and the last picture in Fig. 5-32 (and also happen in Fig. 5-27), it is straightforward to appreciate that islands density decreases with annealing time. So, coalescence processes are continuously taking place. Although nanowires' growth is observed, a tendency towards non-stopping elongation is in general not detected in these particular examples. This behaviour could be consequence of the particular conditions of the experiment. Ar-H_2 atmosphere was interrupted every 5 minutes to allow islands visualization by AFM. After AFM images were taken, sample was introduced again to the furnace at 1000^{o}C to allow further evolution of the islands. However, these very short periods of annealing were probably not enough to ensure a pure Ar-5%H_2 atmosphere and some residual oxygen pressure, higher than the habitual, most likely remained. Consequently, the concentration of oxygen vacancies in CGO nanoislands might be lower than that typically achieved after the purge always carried out prior to annealing. However, despite the lack of extremely long wires, the main features characterizing these nanoislands' evolution and kinetics are distinguished. Furthermore, it must be considered that as islands' size increases, the kinetic limitations become more important. As a result, non-equilibrium islands' morphologies remained (Fig. 5-27c, Fig. 5-32d).

In general, it is found that wires' size, and therefore its in-plane anisotropy, might depend on the sample. A priori, two basic factors could explain this behaviour. In one hand, the particular energy of the system (surface energies, strain energy, etc.) might lead to formation of longer and larger nanoislands as a path towards minimization of the total energy of the system. In this case, the shape and size of nanowires would be thermodynamically determined and, hence, all islands of the same volume are expected to exhibit the same lateral aspect ratio. On the other hand, we might be in a situation were kinetic processes dominate over thermodynamic

ones. Thus, island size and shape would not reflect its equilibrium structure, but would be consequence of kinetic limitations and possibilities (atomic diffusion, etc.). In this case, a broad distribution of wires' lengths could be observed for a given island volume. Relations observed between wires' height and short axis' width (Fig. 5-15) and between their size D and lateral aspect ratio c (Fig. 5-17) suggest thermodynamically-controlled islands' shapes and sizes. However, thermodynamic calculations based on the energies involved on the formation of these islands are required to prove it, as it will be carried out in chapter 6.

Nonetheless, kinetic mechanisms are in any case required to evolve towards equilibrium structure. Although distinct processes characterizing nanowires' evolution have been determined, the exact kinetic mechanisms controlling this evolution of (011)CGO nanoislands on LAO substrates is still unknown at present. It must be a complex issue which possibly comes already influenced by the proportion of (011)-nuclei. However, it must be kept in mind that the number of oxygen vacancies might also play a non negligible role (see also section 4.3). Level of vacancies can be controlled through Gd-doping and through oxygen pressure; moreover, we have shown that a large amount of oxygen vacancies must exist at the interface as consequence of the dissimilarity between the fluorite CGO and the perovskite LAO. The sum of both processes, (011)-nuclei and oxygen vacancies concentration, seems to be crucial for the ultrafast evolution of these (011)-nanostructures. Thus, a complicated scenery emerges where in fact separation between thermodynamic and kinetic processes becomes very difficult. Nevertheless, in the next chapter we will show that most of these behaviours (anisotropic shape, continuous elongation, etc.) can be predicted by thermodynamic considerations.

However, what it is experimentally unquestionable is that (011)-nanowires display an extremely fast ripening with respect to (001)-nanodots. This suggests that a new evolution mechanism (probably based on the sum of many individual processes) has becomes active, which distinguishes their diffusion behaviour and which is worth of being investigate. After reported results, two main reasons could essentially trigger this enhanced mobility: the anomalous (011) orientation of nanowires or the use of a reducing atmosphere, which promotes oxygen vacancies formation and, consequently, an increase of atomic diffusion. Next section 5.4 will be devoted to combined experiments with different oxygen pressure in order to discern the source of contrast between both CGO nanostructures. However, we will first investigate the role of temperature on nanoislands' formation and evolution.

5.3 The role of temperature in (011)CGO nanoislands evolution path

The role of growth temperature in mobility was roughly investigated in section 4.3.2.4. Here, we focus on the evolution path followed by the system CGO/LAO in reducing atmosphere as function of time at 600ºC, 800ºC and 900ºC, respectively. All samples exhibited in this section were prepared from 0.008 M precursor solution and annealed in Ar-H_2 at the specified temperature and time.

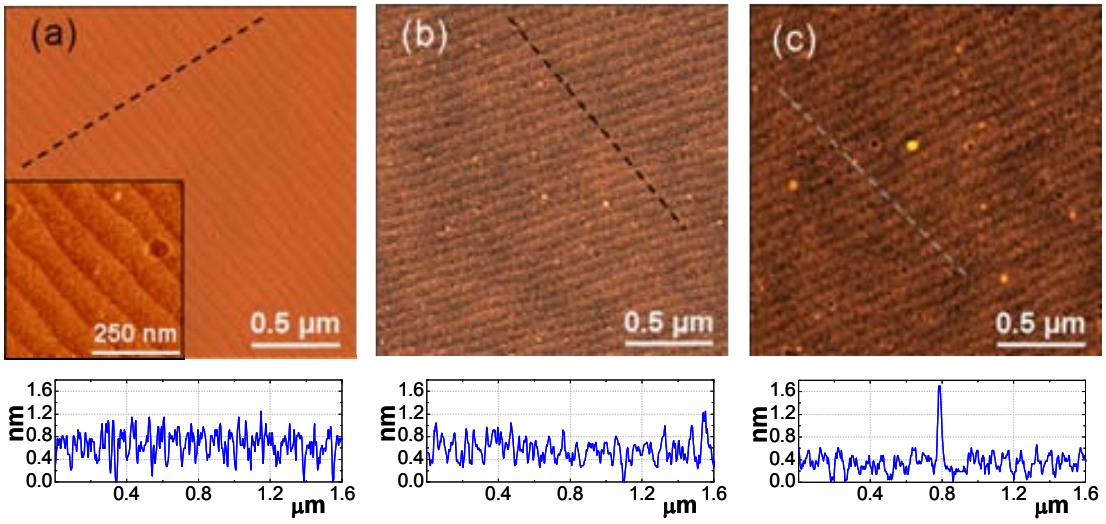

Fig. 5-37: AFM topographic images showing the evolution path at 600ºC in Ar-H_2 of CGO/LAO after 30 min (a), 2 hours (b) and 12 hours (c) annealing. Metal-organic precursor solution of 0.008 M was used.

As proved through the sequence displayed in Fig. 5-37, 600ºC is a too low temperature for the formation of well-defined 3D islands, at least for the investigated annealing times (12 h). At this temperature, thermal energy available to the system seems to be not enough to surmount, in general, nucleation events and, thus, complete epitaxial growth is not achieved. Past 8 hours of heat treatment, most of the material still remains as the amorphous layer formed after the organic removal (typically at 300ºC-400ºC). The use of highly diluted solutions allows us to distinguish the lattice steps under the amorphous layer, which have an average roughness rms~0.21 nm. However, by then, the formation of few stable nuclei of ~(1.2±0.3) nm height and density just ~2.7 islands/µm^2 starts to be observed. After 12 h of heat treatment, the situation remains fairly similar. So, it becomes already evident that the use of reducing atmosphere is not the only driving force leading to ultrafast kinetics. Achievement of high atomic diffusion depends not only on the atmosphere, but also on temperature. The former (atmosphere) gives the number of positions available for atoms to jump (vacancy concentration); whereas the latter (temperature) determines the probability to surmount the potential barriers between distinct sites. The jump of an atom from their present position to another one is a thermally activated process, like in ionic conductors where ionic conductivity σ follows an exponential law with

temperature, i.e. $\sigma = \sigma_o \exp(-\Delta E/kT)$ [223]. Nevertheless, despite samples processed at 600ºC do not satisfy our present purpose of generating nanostructured templates, they arise as a promising route to flatten surfaces, especially of rough samples.

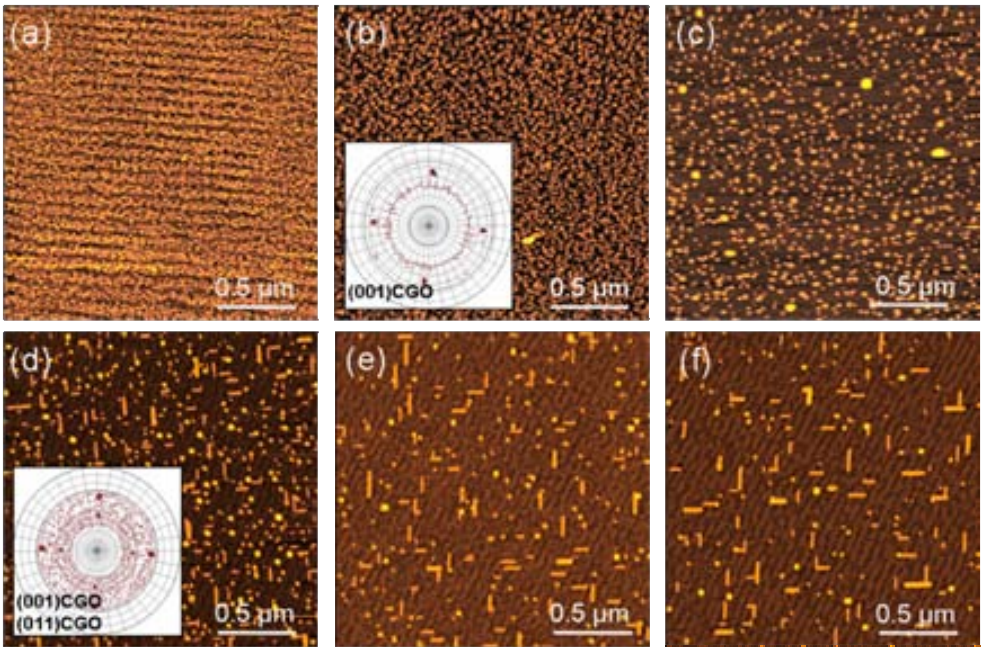

Fig. 5-38: CGO interfacial nanoislands formation and evolution on LAO substrates at 800ºC in Ar-H_2, from 0.008M precursor solution. Different snapshots correspond to annealings of 30 min (a), 1 h (b), 4 h (c), 8 h (d), 36 h (e) and 46 h (f). (111)-CGO pole figures are also displayed in some cases. Notice that isomorphic dots are initially the dominant island population, but later anisotropic wires become the most important one.

Much more interesting and rich are templates prepared at 800ºC. Different snapshots of the evolution path followed by interfacial CGO nanostructures processed at this temperature are displayed in Fig. 5-38, all them also correspond to the same sample. Contrary to ultrafast island formation at 1000ºC, an amorphous layer homogeneously covering all substrate with rms~0.39 nm is still present after 30 min of treatment at 800ºC (Fig. 5-38a). If any small CGO nanodot is already present, it is masked by AFM resolution limits. After 1 hour annealing, the formation of the first nuclei is already appreciated, with equivalent diameter and height determined from AFM images as ~(20±6) nm and ~(2.2±0.5) nm, respectively; and very high density, ~550 dots/µm^2 (Fig. 5-38b). They are isomorphic in lateral shape and XRD^2 pole figure analysis reveals that at least most of these nanoislands are (001)-oriented. Therefore, tendency to promote (011) nucleation in front of (001) in reducing atmosphere is drastically modified when growth temperature is reduced. However, the observed landscape changes after 8 h of heat treatment (Fig. 5-38d), when the two typical distinct morphologies of interfacial CGO nanostructures, i.e. dots and wires, start to be simultaneously visible. Even though, nanodots are still the major population. Their respective densities are 108 dots/µm^2 vs. 37 wires/µm^2. Isomorphic islands are ~(30±8) nm in diameter and ~(11±4) nm high; whereas anisotropic

structures long and short axis are ~(79±27) nm and ~(27±4) nm, respectively, and ~(10±4) nm in height. The beginning of this shape transition also becomes evident through XRD^2 measurements, where the existence of a relatively important fraction of (011)-crystallites is detected, though (001)-nanostructures are still present.

Given that a sudden transformation of crystallographic orientations is not expected, the apparition of nanowires can be explained if one considers that a tiny percentage of (011) nuclei is also present in the template since first evolution stages at 800ºC (small enough to be detected by XRD^2 and below AFM resolution limits). As described above, (011)-nanoislands experience fast growth rate and a great tendency to engulf nanodots lying around. Thus, (011)-nanowires growth takes place at expenses of (001)-dots. Although isomorphic dots were initially majority, after long heat treatments the relative amount of crystallographic populations is inverted and the ratio wires/dots, i.e. (011)/(001), increases unstoppably. There is a process of coarsening competition among (001) and (011) nuclei, which is always won by (011)-islands even if very long annealings are required when their initial concentration is vanishing small. Even tough, in the present case, after 46 hours (Fig. 5-38f) an exclusive (011)-wires population is still not achieved in the sense that small fraction of (001)-crystallites is still detected by XRD^2 measurements.

At 900ºC, atomic mobility in Ar-H_2 is higher than previous examples at lower temperatures, but still lower to that achieved at 1000ºC. A mixed population of (001)-dots and (011)-wires is obtained after 30 min of annealing at 900ºC in reducing atmosphere, as it is shown in AFM images and XRD^2 (111)-CGO pole figure shown in Fig. 5-39a. The undulation observed at top of nanowires in the displayed profile is due to a misalignment between the sample and the AFM line scans. After 1 hour of heat treatment, both morphological shapes are still observed through AFM images, though mainly (011)-CGO orientation is detected by XRD^2 (Fig. 5-39b). (001)-dots' density is reduced by a factor ~2.2, at the same time that wires' density is decreased a factor ~1.8 with respect to the same sample treated 30 min less. The former reduction is explained through the engulfment of dots by wires; whereas the latter is due to the coalescence and reconstruction of nanowires' labyrinthine structures into a larger nanowire. The mean volume of wires increases essentially due to elongation because width and height remains fairly constant. After 2 hours annealing at 900ºC (Fig. 5-39c), a nearly exclusive wires' population is achieved; just very few dots are still observed. At this stage, the distribution of wires' lengths is rather broad, with values ranging from ~70 nm to ~785 nm. Again, the size of short axis width is kept quite constant and in any case overcomes ~28 nm. The small wires show a minimum height of ~4 nm, whereas the largest ones do not exceed ~13 nm height.

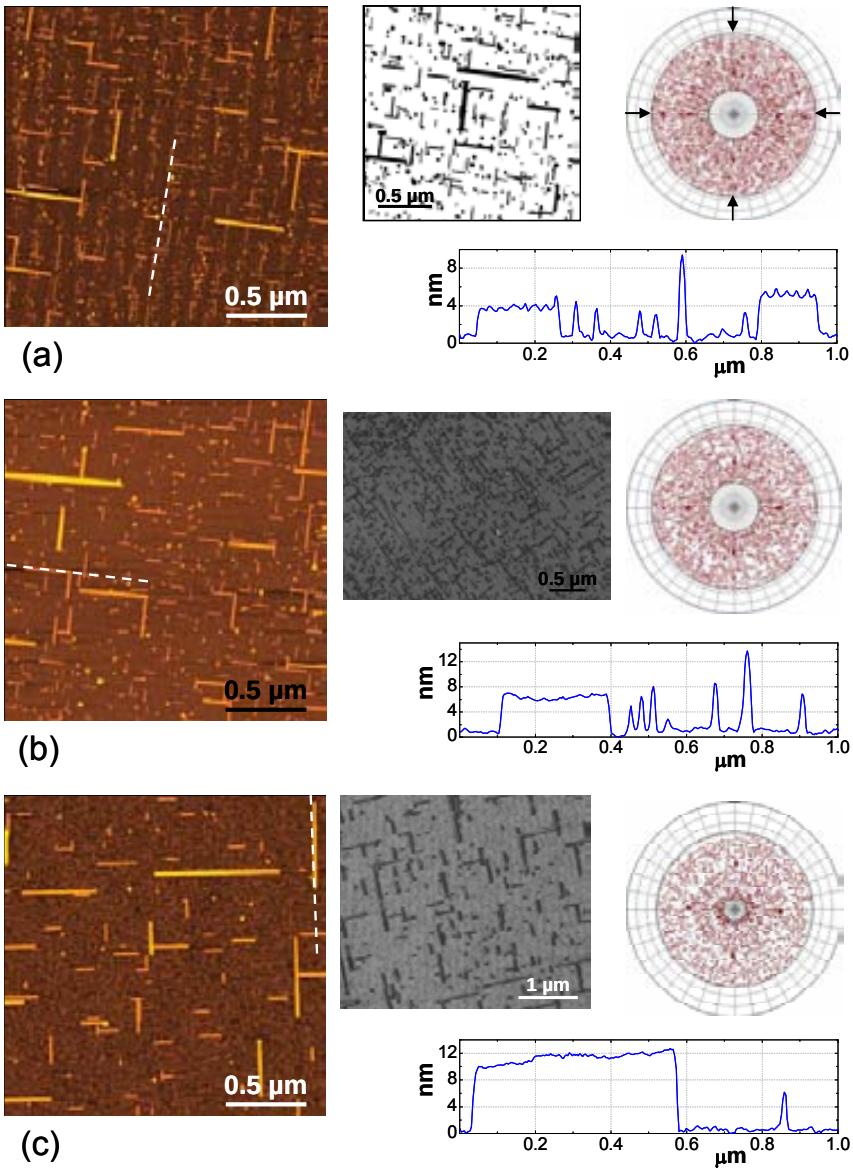

Fig. 5-39: CGO interfacial nanoislands formation and evolution on LAO substrates at 900ºC in Ar-H_2. Different snapshots correspond to annealings of 30 min (a), 1 h (b) and 2 h (c). (111)CGO pole figures are also displayed. Initially, a mixture of dots and wires was grown; but after subsequent annealings an exclusive wires' population is observed. Precursor solution of 0.008M was used.

Therefore, these experiments point out that (011)-crystallites can also nucleate at temperatures below 1000ºC, but in a lower proportion. In spite of not being initially the main crystallographic orientation, (011)-nanoislands can become the dominant one through its ability to absorb dots, which competes and wins over coarsening phenomena between (001)-islands. Fig. 5-40 shows the evolution as function of the annealing time of the XRD^2-intensity of (011)-nanoislands with respect to the sum of the intensities corresponding to (001) and (011) crystallographic orientations. Results refer to heat treatments at 800ºC, 900ºC and 1000ºC; all cases in reducing atmosphere and using a precursor solution of 0.008 M. It is appreciated that as

lower is the growth temperature, longer heat treatments are required to achieve a template with predominant (011)-nanowires' population.

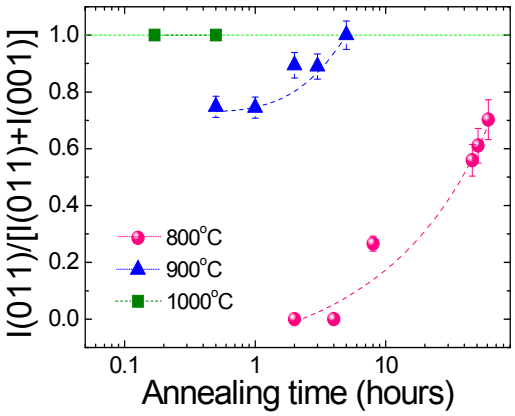

Fig. 5-40: Evolution of the fraction of crystallographic orientations XRD[2] intensities I(011)/[I(011)+I(001)] as function of annealing time at different temperatures: 800°C (●), 900°C (▲) and 1000°C (■).

Once shown that it is possible to achieve a nearly exclusive (011)-nanowires population after sufficiently long treatments at low temperatures, it still remains unknown why (011)-crystallites nucleated. All distinct experiments point to atomic mobility as the driving force controlling the ratio of islands nucleating with (001) and (011) crystallographic orientation. It has been proved that both high oxygen pressure (i.e. low concentration of oxygen vacancies) and reduced temperature lead to a decrease of atomic mobility, and both also enhance the probability of nucleating (001)-dots. Growth temperature has already been widely used to modify the degree of interfacial coherence in many systems, such as some ReBCO-like thin films [261]. It is known that low atomic mobility (generally achieved through growth at low temperature) normally enhances the formation of coherent interfacial islands [194]. There exists a mobility threshold for the formation of misfit dislocations at the interface so that mobility is usually not enough at low temperatures to generate them. Since dislocations are difficult to create under these conditions, we should expect that reduced mobility during growth would increase the elastic energy of the system. So, the energy of the island should be mainly dominated by this energetic contribution. Under these conditions, nucleation of islands with lower misfit would be more favourable than those with high misfit. Accordingly, (001)CGO nanoislands should be formed at low temperature and/or high $P(O_2)$.

Contrary, at high atomic mobilities (higher temperature or reduced $P(O_2)$), more misfit dislocations are formed and, thus, semi-coherent structures should be promoted. In this case, (011)-crystallites should stabilize easier than (001) because their high elastic energy largely decreases when misfit dislocations are formed. To observe this phenomenon the total energy of both islands should be similar, which seems to be the case in CGO. Moreover, the interface energy of (001)CGO||(001)LAO and (011)CGO||(001)LAO might be fairly similar since it is so

easy (through temperature or atmosphere modifications) to induce the nucleation of one or the other. Also, it seems that we are in the right range of temperature and oxygen vacancies to modify the balance between competing terms in the nucleation energy.

All these arguments only refer to the nucleation energy, i.e. the energy of the first stable nuclei during growth. After these nuclei are formed, the kinetic evolution can be completely different in both cases. Everything seems to suggest that the number of stable (011)-nuclei decreases when temperature is reduced at low $P(O_2)$ and when $P(O_2)$ is increased. However, despite less (011)-nuclei are stabilized at low temperatures, formation of highly elongated nanowires can rapidly be achieved under conditions known of ultrafast mobility (high temperature and reduced $P(O_2)$). As an illustration, Fig. 5-41 displays the AFM images corresponding to a template processed at 800ºC in Ar-H_2 for 2 hours and then submitted to 30 minutes annealing at 1000ºC in reducing atmosphere as well. After first thermal treatment at 800ºC, an exclusive population of (001)-isomorphic dots was obtained (Fig. 5-41a), like the one reported in Fig. 5-38. In subsequent annealing at 1000ºC, nearly all islands observed by AFM and detected by XRD[2] correspond to (011)CGO nanowires (Fig. 5-41b). So, a template with a nearly exclusive population of (011)-nanowires has rapidly developed (30 min) despite the minority percentage of this population at first evolution stages. Thus, it is important to distinguish between nucleation and evolution, which is strongly linked to kinetics.

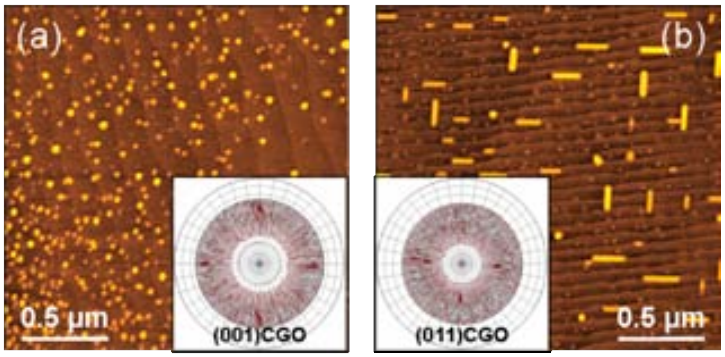

Fig. 5-41: AFM topographic images and XRD[2] (111)-CGO pole figures showing the preferential nucleation of (001)CGO dots at 800ºC (2h, Ar-H_2) (a) and subsequent annealing of 30 min at 1000ºC also in reducing atmosphere (b), after which mainly interfacial (011)-wires are observed.

Nevertheless, after reported results it cannot be completely ruled out that the initial ratio between (001) and (011) stable nuclei is always the same, independently of the nucleation temperature. In this case, kinetic differences between templates would just be attributed to the dependence of atomic mobility with temperature. On the other hand, there are experiments of metal growth on (001)STO single-crystals which show that nanoislands crystalline orientation can be tuned through previous reconstruction of substrate surface [21, 262]. However, while exhaustive studies have been performed on STO surface reconstructions depending on different process conditions; for LAO substrates is even not exactly known which of the charged

terminations, $(LaO)^+$ or $(AlO_2)^-$, is obtained after annealing in present growth conditions. First XPS studies we have performed in collaboration with the group of Dr. Martín Gago at ICMM-CSIC indicate very little differences between bare LAO single-crystal substrates treated in O_2 or Ar-H_2 (just differences in C and O arise indicating that Ar-H_2 atmosphere reduces the contamination of the surface). Thus, a priori it seems that differences in substrate might not be the present cause of distinct crystalline orientations. Nevertheless, LEED measurements are planned to study in detail possible reconstructions of LAO surfaces under different processing conditions.

Independently of the mechanism of nucleation, in this section we have shown that (011) stable nuclei can also nucleate below 1000°C in reducing atmosphere. However, high temperatures are required to achieve ultrafast atomic diffusion in (011)-nanowires or in processes which involve this type of nanoislands.

5.4 The role of atmosphere in CGO nanoislands evolution path

Once proved that temperature plays an important but not essential role in the observed contrast between (001) and (011) nanostructures, let's focus on the study of atmosphere responsibilities for islands' formation and evolution. The key point is to experimentally investigate the mechanisms leading to the extraordinary mobility of nanowires, trying to discern if it is related to their particular crystallographic orientation or due to low oxygen pressure atmosphere. Consequently, two experiments were designed based on atmosphere's modification. Since it is known that at 1000°C we can select the preferential crystallographic orientation of nanoislands through oxygen pressure adjustment, we grew one sample in Ar-5%H_2 and another in O_2, and then we interchanged atmospheres and carried out further annealings. Both samples were prepared from 0.008 M precursor solution.

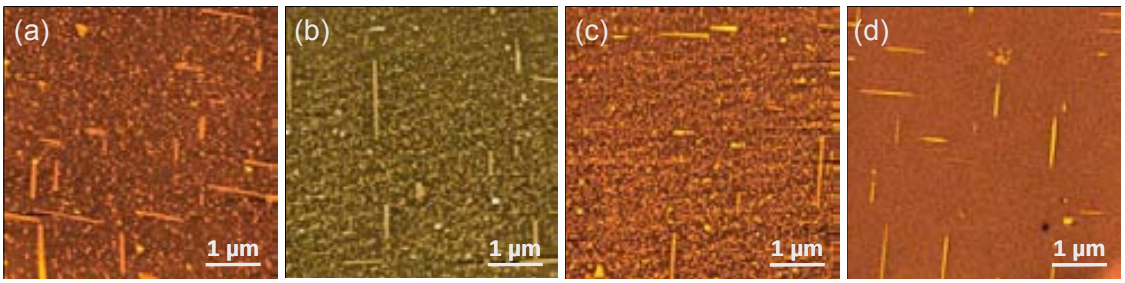

Fig. 5-42: Combined atmosphere experiment performed at 1000°C: 30 min of heat treatment in Ar-H_2 to ensure nucleation of (011)-islands, objective achieved since presence of wires is observed (a); posterior evolution in O_2, where no changes are detected after annealings of 4 h (b) and 8 h (c); and final annealing of 30 min in Ar-H_2, during which most dots are rapidly engulfed by wires (d).

AFM image displayed in Fig. 5-42a corresponds to a very initial evolution stage of a template grown in Ar-H_2 atmosphere, where still dots and wires are present and, particularly,

more of the former than the latter. A non exclusive presence of wires was desired to easily observe the evolution path followed by nanostructures, as it is simplest to detect nanowires growth at expenses of nanodots than through their reconstruction (basically because dots' extinction is simplest to visualize than elongation). Nearly no changes are appreciated in subsequent annealings in oxygen atmosphere for heat treatments as long as 8 hours. Both types of nanostructures are still present with equivalent sizes, densities and distribution as it is proved in Fig. 5-42b and c. Just a slight tendency of (001)-nanodots to diffuse towards nanowires is guessed from the nanodots' voids surrounding wires, which extend up to 60-80 nm from the wires (see detail in Fig. 5-43). Thus, despite ultralow mobility of islands under these conditions, wires continue to act as capturing centres of (001)-nanodots but with much lower efficiency than in Ar-H_2.

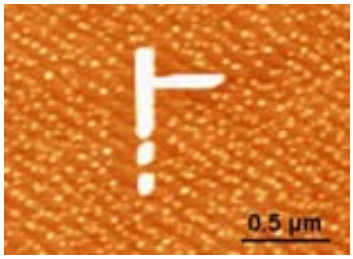

Fig. 5-43: AFM topographic image of a CGO/LAO template with wires and nanodots. Notice the nanodots' void surrounding the wires, illustrating the tendency of (011)-wires to absorb (001)-dots.

If dominant feature on island's mobility was just their particular crystallographic orientation, increase of nanowires at expenses of dots should be clearly observed, independently of the annealing atmosphere. This is not the present case, where slow mobility is perceived even tough the presence of (011)-nanostructures, as exemplified by the observation of wires. Therefore, crystallographic orientation cannot be the driving force, or at least the only motor, to explain the ultrafast mobility of CGO nanoislands; atmosphere and the number of oxygen vacancies that it induces is also a crucial parameter. This role is further stressed when then treating the same sample in Ar-H_2 for 30 minutes at 1000^{o}C after having remained 8 hours in pure oxygen atmosphere. A template with unique wires' population is obtained (Fig. 5-42d), as would be expected for a template treated in reducing atmosphere for more than 30 minutes. At the same time, the achievement of this stage proves that these results are not sample dependent. The lack of evolution of nanowires in oxidizing atmosphere can be related to an inversion of the concentration of oxygen vacancies at the surface, indicative that the concentration of oxygen vacancies in O_2 (O/M~1.95) does not provide the enhanced mobility achieved in reducing atmosphere (O/M~1.85) [231].

So, fast atomic mobility associated to Ar-H_2 can be attributed to enhanced oxygen vacancies formation by using a reducing atmosphere, helped by Gd-doping (section 4.3.2).

However, from that statement it could be derived that reducing atmosphere is already enough to promote high mobility of CGO nanoislands. In order to investigate that point, the inverse experiment was carried out. Fig. 5-44a corresponds to a typical template processed 30 min at 1000°C in O_2, with isomorphic (001)-dots disposed along terraces of the substrate. Their (001) crystallographic orientation was confirmed by XRD[2] measurements. If then this template is annealed in Ar-H_2 atmosphere, just slow coalescence processes are observed between isomorphic nanodots lying within the same terrace for treatments as long as 5 hours (Fig. 5-44b and c). Therefore, there is just a slight increase of dots' size at the same time that its density decreases; the same evolution path followed by self-organized nanodots processed in O_2 showed in section 5.2.1. Till that moment, no trace of fast growth typically displayed by nanoislands nucleated and annealed in reducing atmosphere is observed. Surprisingly, the landscape drastically changes after 10 h of heat treatment in Ar-H_2 when extremely elongated nanowires suddenly develop. Fig. 5-44d shows the corresponding snapshot; more details are displayed in Fig. 5-45. These CGO nanowires are ~13 nm high, ~89 nm width and can reach lengths of 30 µm, which results into lateral aspect ratios as amazing as $c=(b/a)^{½}=18.4$. Notice that according to our definition of c, such values indicate that wire's length is 337 times larger than its width. FESEM images like ones in Fig. 5-45a and b revealed that these nanowires are homogeneously distributed over the substrate. Notice that these nanowires are perfectly aligned along substrate soft directions [100] and [010] constituting percolating intricate structures of orthogonal islands. A special tendency of these wires to join through their ends in 90° configuration is not observed, like if impingement between wires occurred by chance.

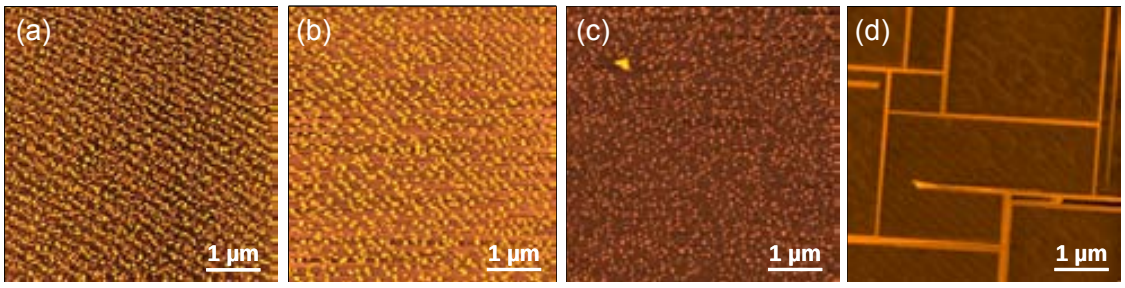

Fig. 5-44: Combined atmosphere experiment performed at 1000°C: 15 min in O_2 to ensure nucleation of (001)CGO nanoislands (a), and posteriors treatments in Ar-H_2 of 1 h (b), 5 h (c) and 10 h (d). Sudden formation of nanowires is observed after annealing (001)-nanodots 10 h in Ar-H_2.

The most outstanding feature of these nanowires is that they have the crystallographic orientation (001)CGO||(001)LAO, as it has been determined from XRD[2] measurements (Fig. 5-45e). Thus, in contrast to (011)-nanowires, these (001)-nanowires are biaxial isotropic strained and exhibit isotropic surface energy facets. Hence, driving forces suggested for the elongation of (011)CGO wires would not apply to the present case. TEM analyses are required to prove these details. However, thermodynamic analyses presented in next chapter will

effectively show the possibility to obtain elongated (001)CGO nanostructures once a critical island's size is achieved [28, 68].

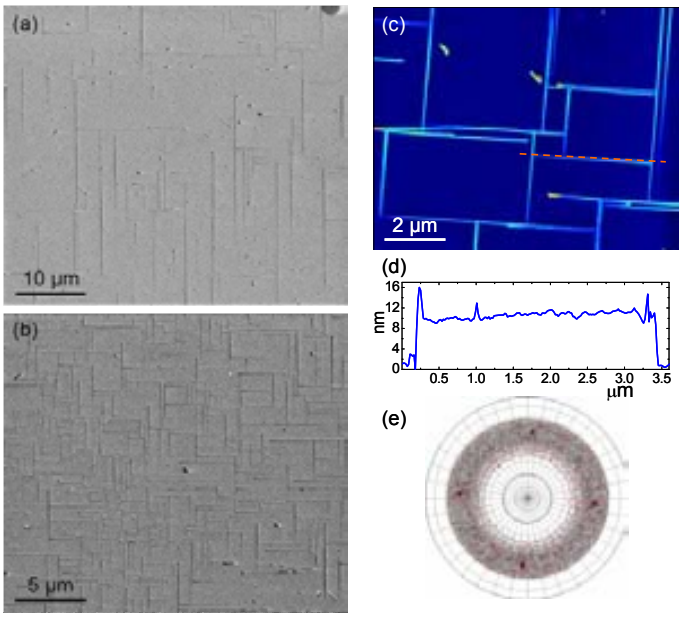

Fig. 5-45: (001)CGO nanowires on (001)LAO substrate formed at 1000°C after 15 min anneal in O_2 and posterior treatment (10 h) in Ar-H_2 (corresponding to Fig. 5-44d): FESEM images (a, b), AFM (c), profile of a wire (d) and XRD[2] measurements confirming the crystallographic orientation (e). Notice the extremely length of these nanowires, which can reach the extreme length of~30 µm (a).

The unexpected formation of (001)CGO nanowires hints that we have found a particular combination of growth conditions that can promote the coarsening of stable (001)CGO nanodots, perhaps because of an increase of the concentration of oxygen vacancies in the CGO fluorite structure after long annealings in reducing atmosphere. The formation of such extraordinary long wires definitely deserves further investigation. Higher temperature annealings (>1000°C) could be another and easier strategy to enhance the coarsening of (001)CGO dots, yielding to the rapid formation of elongated (001)-wires. Existence of unstable ripening above a critical temperature has already been proved by statistical models applied to heteroepitaxial systems of quantum dots [60].; hence, there might as well exist a set of growth conditions were (001)-nanodots are not stable any more.

Summarizing, reducing atmosphere and vacancies created through it seems to be a key point to achieve ultrafast mobility in CGO/LAO system through the enhancement of coarsening mechanisms. Elongated (011)-nanowires rapidly form right after nucleation in Ar-H_2 (achieving lengths of few µm in <1 h), but their evolution is nearly interrupted in O_2. On the other hand, after extremely long annealings in reducing atmosphere (~10 h), (001)-nanodots can overcome coarsening barriers leading to the formation of (001)-nanowires. Nonetheless, we will show in

next chapter that other factors might influence as well islands' formation (interaction among islands, thermodynamics of the system, etc.).

5.4.1 Influence of gas flow on the formation of CGO-nanostructures

Reducing atmosphere (and high temperatures) has just been proved to be indispensable for the ultrafast mobility of CGO nanoislands. Let's now roughly investigate the influence of gas flux on islands' formation.

All templates shown up to now were processed in a gas flow rate of 0.03 l/min. In oxidizing atmosphere, no significant differences are observed for oxygen flux rates as high as 0.6 l/min, as it is exemplified in Fig. 5-46 where both cases are compared: 0.03 l/min (a) and 0.6 l/min (b). These AFM topographic images effectively indicate that very similar evolution stages are reached, with similar dots' sizes (within AFM resolution limits) and distributions, independently of O_2 flux rate. After the observation of several templates with interfacial (001)CGO nanodots, we can attribute differences in size between the dots of both images to a higher influence of the tip in image (b).

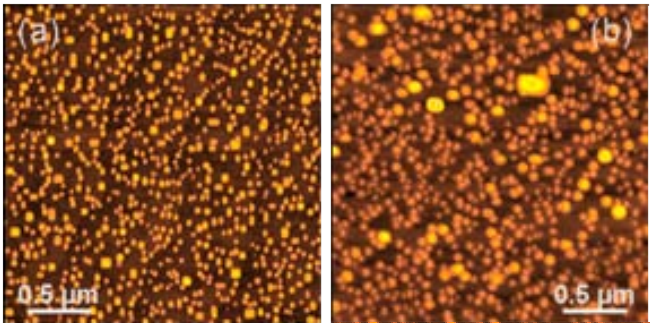

Fig. 5-46: AFM topographic images of CGO/LAO templates prepared from 0.008M solutions at 1000°C for 30 min in constant O_2 flux of 0.03 l/min (a) and 0.6 l/min (b). No significant differences are observed between dots' characteristics, within AFM tips' convolution.

Contrary, Ar-5%H_2 flow influences islands' evolution in a way that mobility increases with flow rate. Fig. 5-47 compares the case of a template (a) prepared at 0.012 l/min with another one processed at 0.6 l/min (b). For the latter the mobility is so high that nanowires are even not found.

So, gas flow is signalled as another parameter enhancing the evolution rate of (011)CGO nanoislands. Dependence of film growth on gas flow is in general not well-established. It has been empirically suggested that growth rate of YBCO thin film depends on the square root of gas flow, among other factors [263], which indicates the fast mobility can be achieved as gas flow increases. Hence, the observed gas flow dependence becomes another example of the relevance of kinetic effects on the evolution of nanoislands coarsening. Some

dependence on gas flow could suggest that the concentration of oxygen vacancies in (011)CGO islands is not uniform through the island's volume, i.e. a gradient in its concentration exists from the surface towards the inner part. Let's recall that oxygen vacancies must necessarily exist at the interface as consequence of the dissimilarity between the fluorite CGO and the perovskite LAO. A higher gas flow would increase the concentration of oxygen vacancies at the surface and hence in the whole volume, which might lead to high atomic mobility. Similar processes might be involved in the formation of (001)-nanowires after long annealings in Ar-H_2.

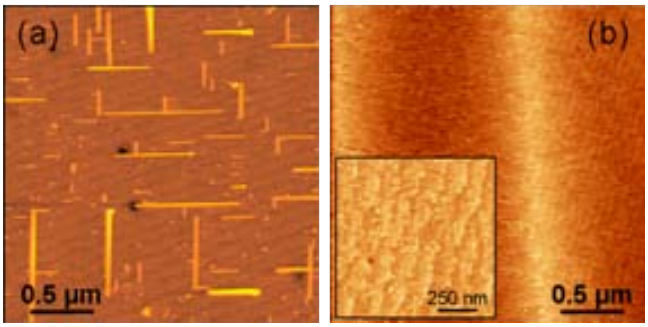

Fig. 5-47: CGO/LAO templates prepared from 0.008M solutions at 1000°C for 30 min in constant Ar-H_2 flux of 0.012 l/min (a) and 0.6 l/min (b). Notice that no wire is observed in (b).

5.5 Summary and conclusions

In the present chapter we have investigated in detail CGO/LAO system. The capacity to tune lateral aspect ratio of interfacial CGO nanoislands through growth conditions has bring us to use this heteroepitaxial system as a model to study the growth of strain-induced oxide nanoislands. Initially, we divided CGO nanostructures in two main groups depending on their in-plane aspect ratio, isomorphic for the case of nanodots and elongated for nanowires. At first approximation, this classification is equivalent to separate CGO nanoislands depending on oxygen pressure at which they were processed (at 1000°C).

Structural characterization based on XRD[2] and TEM analyses have pointed out that CGO nanodots (i.e. nanoislands processed in O_2) grow on LAO single-crystals according to the epitaxial relation (001)CGO[110]||(001)LAO[100]. A pretty good matching of cations sublattices results into a lattice mismatch of just ε~-1%; however, large amount of oxygen vacancies must be created at the interface due to the structural dissimilarities between the substrate perovskite and the fluorite. TEM images revealed that isomorphic (001)CGO nanodots are nanopyramids with square base and truncated for all investigated sizes. All four lateral facets correspond to (111)-CGO planes, the CGO planes with lower surface energy. It has been determined that the lateral growth of (001)CGO nanodots is ~4 times faster than their vertical growth.

A completely different situation describes nanowires. The most outstanding behaviour, and probably the one triggering most of their particularities, is its singular crystallographic orientation. Nanowires grow (011)CGO||(001)LAO, configuration which implies two distinct in-plane growth directions. On one hand, CGO[0-11]||LAO[010], which is the same interface observed for the case of (001)-nanodots with ε~-1%. On the other hand, CGO[100]||LAO[100]. To describe the epitaxial growth in this direction (which in the frame of lattice mismatch theory bears ε~-30%) we have based on the domain matching epitaxy model (DME). Two CGO fluorite cells fit pretty well three LAO perovskite cells and a misfit dislocation exists in each domain; as a result the residual misfit in this growth direction would be ε~+5%. Thus, (011)-nanowires are submitted to anisotropic strain with also different sign, compressive or tensile depending on the in-plane growth direction.

Elongation of (011)-nanowires occurs in the direction of lowest mismatch, i.e. CGO[0-11]||LAO[010]. Elongating in this direction island also extends the lateral facets of lower surface energy, (111). Nanowires' short ends are limited by higher energy planes (001). TEM images have also shown that at small sizes (011)-nanowires exhibit triangular cross-section, but flat (011)-planes develop at the top for heights >5 nm. A strong link between nanowires' short axes and their height is observed. Short axis' width is kept fairly constant for all investigated situations (≤50 nm); contrary, their long axes can achieve microns of length. A general trend of the increase of the lateral aspect ratio as island's base area increases seems to be followed by all nanowires, suggesting that its shape is thermodynamically dominated.

Hence, (001)CGO nanodots grow under biaxial isotropic stress and exhibit isotropic surface energies in all lateral facets. In contrast, (011)CGO nanowires are anisotropically strained and the surface energies of lateral facets are also anisotropic. So, thermodynamic analyses must be carried out to know if their particular energies (surface energies, strain energy, etc.) can actually explain these differences in shape.

The evolution of (001)-nanodots and (011)-nanowires in the atmosphere where they were nucleated has also been investigated. Independently of the annealing period, (001)CGO dots are ordered in rows resulting into highly ordered templates. Nanodots are confined in the central part of substrate terraces despite their height is ~20 times higher than the lattice steps themselves. The mechanism leading to such efficient confinement seems to be the dissimilarity between the fluorite CGO and the perovskite substrate, which results into high energetic interfaces at step edges. In each single terrace, coarsening phenomena are also limited and a homogeneous mean separation is observed between dots aligned in a terrace. As a result, regions with local 2D order are observed. The lack of coarsening mechanism suggests that these (001)CGO nanodots are perhaps in equilibrium state. Thermodynamic analyses are required to prove it.

Again, a completely distinct landscape has been observed in templates with (011)-nanowires and processed at low oxygen pressure (Ar-H_2) and high temperature (1000^{o}C). The formation of extremely long nanostructures in just minutes of heat treatment proves the extraordinary mobility of these nanoislands. In this case, the localization of nanowires is completely determined by substrate soft axes [100] and [010]; i.e. all nanowires are aligned parallel to these directions. Different static AFM and TEM snapshots point out remarkable tendency of nanowires to join in orthogonal configuration, i.e. short-long axes union and especially through their short axes forming a 90^o angle. In contrast, two nanowires are never observed to join through their long axes. As a result, intricate nanolabyrinthine groups form after the junction of orthogonal nanowires oriented along substrate [100] and [010] axes. In advanced evolution stages, nanowires are found to reconstruct into larger nanoislands keeping its short axes and height fairly constant. The volume of nanowires not only increases because of the incorporation of attached nanowires but atomic diffusion between (011)-nanoislands has also been observed. Moreover, a high tendency of (011)-nanowires to absorb (001)-nanodots from the surrounding has been detected too. It has also been observed that there exists a moment when reconstruction of larger structures might not lead to the formation of longer nanowires but irregular polyhedral islands. Kinetic-limited processes have been suggested as the mechanism yielding to these situations.

Hence, whereas isomorphic (001)CGO nanodots display very limited coarsening, (011)-nanowires continuously coalesce and reconstruct into longer nanoislands. So, it seems that dots have reached their equilibrium size, whereas the system with nanowires is continuously in evolution, probably searching for a lower energy configuration. Thermodynamic studies should be carried out to determine the equilibrium size of both types of interfacial nanoislands. It would enable to establish if (001)-dots are stable or kinetically limited and, on the other hand, if (011)-nanowires are kinetically controlled or their behaviour is thermodynamically pushed. Moreover, theoretical studies should also be required to determine the interaction between islands.

Reducing atmosphere is essential for the nucleation of (011)-nanoislands, but the proportion of stable (011)-nanoislands after nucleation has been observed to decrease with temperature. However, despite not being even initially detected (800^{o}C) or correspond to a small fraction (900^{o}C), (011)CGO nanowires become the dominant population after long enough annealings in Ar-H_2 due to their ultrafast kinetics and ability to swallow (001)-nanodots. On the other hand, reducing atmosphere is not the exclusive condition to achieve ultrafast mobility; high temperatures are as well required. The last step has been to distinguish between the influence of (011)-crystallites and Ar-H_2 atmosphere on the ultrafast mobility of these nanoislands. Experiments with combined atmosphere for nucleation and evolution have

showed that (011)-nanoislands just evolve very rapid in Ar-H_2 and not in O_2, indicating that large amount of vacancies is required for high diffusivity. Ultrafast mobility is neither achieved in Ar-H_2 in templates with (001)-nanodots for annealings as long as 5 h. Surprisingly, after 10 h treatment in reducing atmosphere, coarsening barriers between (001)-nanodots are surmounted and extremely long (001)-nanowires form. Increase of the concentration of oxygen vacancies after long treatments in reducing atmosphere could explain again the rapid mobility achieved in this particular situation. In this case, thermodynamic analyses must indicate if this elongate shape of (001)CGO nanoislands responds to a mechanism of energy minimization or if it is instead kinetically promoted.

We have investigated in detail the growth conditions that enhance ultrafast mobility of (011)CGO nanoislands on LAO substrates. Nonetheless, the mechanism leading to the nucleation of (011)-nanoislands is still unknown. A mechanism based on the energy threshold for the formation of dislocations has been proposed to explain it. In any case, the fact that we can easily control the nucleation of one or other orientation merely through slight modifications of growth conditions suggests that the interface energy of both configurations must be very close.

We can conclude that we have found a very particular set of conditions (basically high temperature and low oxygen pressure) which leads to the nucleation of a singular crystallographic orientation, (011)CGO, in a system already singular because of the presence of dissimilar crystallographic structures (fluorite-perovskite). This particular orientation seems to have a deep impact on the shape and evolution behaviour of the resulting nanoislands which is worth of being investigated through theoretical models in order to discern the features that lead to the formation of extremely long nanowires with well-defined facets and to such distinct situations (as compared to isomorphic (001)CGO nanodots).